J|A|C|S ARTICLES

Published on Web 12/23/2010

Interaction Tensors and Local Dynamics in Common Structural Motifs of Nitrogen: A Solid-State ^{14}N NMR and DFT Study

Luke A. O'Dell,*[,†] Robert W. Schurko,[‡] Kristopher J. Harris,[‡] Jochen Autschbach,[§] and Christopher I. Ratcliffe[†]

Steacie Institute for Molecular Sciences, National Research Council, 100 Sussex Drive, Ottawa, K1A 0R6 Ontario, Canada, Department of Chemistry, University of Windsor, 401 Sunset Avenue, Windsor, N9B 3P4 Ontario, Canada, and Department of Chemistry, 312 Natural Sciences Complex, State University of New York at Buffalo, Buffalo, New York 14260-3000, United States

Received September 10, 2010; E-mail: luke.odell@nrc-cnrc.gc.ca

Abstract: ^{14}N solid-state NMR powder patterns have been obtained at high field (21.1 T) using broadband, frequency-swept pulses and a piecewise acquisition method. This approach allowed the electric field gradient (EFG) tensor parameters to be obtained from model organic and inorganic systems featuring spherically asymmetric nitrogen environments (C_Q values of up to ca. 4 MHz). The advantages and limitations of this experimental approach are discussed, and the observation of ^{14}N T_2 relaxation anisotropy in certain systems is also reported, which can shed light on dynamic processes, allowing motional geometries and jump rates to be probed. In particular, we show that observable effects of dynamics on ^{14}N spectra can be mediated by modulation of either the EFG tensor or heteronuclear dipolar couplings. It is demonstrated that the QCPMG protocol can be used to selectively enhance certain types of nitrogen environments on the basis of differences in T_2. We also present the results of extensive density functional theory calculations on these systems, which show remarkably good correlation with the experimental results and allow the prediction of tensor orientations, assignment of parameters to crystallographic sites, and a rationalization of the origin of the EFG tensors in terms of contributions from individual molecular orbitals. This work demonstrates that ultra-wideline ^{14}N solid-state NMR can, under favorable circumstances, be a straightforward, useful, and informative probe of molecular structure and dynamics.

1. Introduction

The importance and ubiquity of nitrogen in chemistry, biochemistry, and materials science cannot be overstated; however, despite its very high natural abundance (99.63%), ^{14}N is not commonly studied by solid-state nuclear magnetic resonance (NMR). This is primarily due to its electric quadrupole moment ($eQ = 20.44$ mb, 1 mb $= 1 \times 10^{-31}$ m^2),[1] which couples to a surrounding electric field gradient (EFG), resulting in significant perturbations to the Zeeman transition frequencies. For powder samples, this translates to an anisotropic broadening of the spectral line shape for each distinct nitrogen environment. The integer spin number of ^{14}N ($I = 1$) means that both Zeeman transitions are perturbed by this quadrupolar interaction (QI) to first-order. Even for relatively small EFGs (caused primarily by deviations from spherical symmetry in the local electronic environment), powder patterns can be broadened far beyond the excitation and detection limits of standard NMR hardware, and linewidths of several MHz are common. The size of the QI is usually denoted by the quadrupolar coupling constant C_Q, which typically ranges from 0 to ~5 MHz for ^{14}N, the static powder patterns having widths of ca. $1.5C_Q$ at all fields. As well as causing experimental bandwidth issues, the dispersion of the NMR signal across such a wide frequency range is detrimental to the sensitivity, which is already relatively poor due to the low gyromagnetic ratio of ^{14}N (1.93×10^7 rad T^{-1} s^{-1}). Finally, since the chemical shift range of nitrogen (ca. 1300 ppm, or 85 kHz at 21.1 T) is generally far narrower than the quadrupolar broadening, spectral overlap can be highly problematic for samples featuring multiple nitrogen environments.

Considering both the significance of nitrogen and the unique advantages offered by solid-state NMR (such as the ability to probe disordered environments, measure bond distances and angles, and quantify dynamic processes), it is not surprising that much effort has been put into developing new solid-state NMR techniques that can make use of the ^{14}N isotope. For example, recently introduced heteronuclear correlation experiments can provide excellent resolution of different nitrogen sites as well as measurement of quadrupolar parameters,[2−5] though obviously this approach is limited to samples where such strongly coupled "spy" nuclei are available, and analysis of the resultant spectra is not straightforward. Overtone spectroscopy, the direct excitation and detection of the $+1 \leftrightarrow -1$ transition,

[†] Steacie Institute for Molecular Sciences.
[‡] University of Windsor.
[§] State University of New York at Buffalo.

(1) Pyykkö, P. *Mol. Phys.* **2001**, *99*, 1617.
(2) Gan, Z. *J. Am. Chem. Soc.* **2006**, *128*, 6040.
(3) Cavadini, S.; Lupulescu, A.; Antonijevic, S.; Bodenhausen, G. *J. Am. Chem. Soc.* **2006**, *128*, 7706.
(4) Cavadini, S. *Prog. Nucl. Magn. Reson. Spectrosc.* **2010**, *56*, 46.
(5) Gan, Z. *Chem. Commun.* **2008**, 868.

can dramatically reduce spectral widths and improve resolution;[6,7] however, the excitation of this transition is inefficient, and powder line shapes can be difficult to model. Magic-angle spinning (MAS) can improve spectral resolution, provided that the magic angle is precisely set and the spinning speed is very stable.[8] To quantify anisotropic interactions such as the QI or the chemical shift/shielding anisotropy (CSA), however, a broad manifold of spinning sidebands must be acquired and simulated, which is possible only for $C_Q \lesssim 1$ MHz due to experimental bandwidth limitations.[9−13] ^{14}N NMR experiments on single crystals[14] or oriented systems[15,16] are a possibility when such samples are available, but in order to measure C_Q values exceeding 1 MHz from powder samples, acquisition of the ultra-wide-line static powder pattern remains the most straightforward approach. The limited excitation and detection bandwidths of a typical NMR experiment can be overcome by stepping the transmitter frequency and recording the spectrum in a piecewise fashion. Such an approach was combined with slow sample rotation (RotIsseRIe)[17] to record one-half of the ^{14}N powder pattern from silicon nitride ($C_Q \approx 2.1$ MHz).[18] However, the very narrow excitation bandwidth of the spin−echo pulse sequence used in this study makes such an approach very time-consuming. Large C_Q values may also be measured at fixed transmitter frequencies using the STEAMER methodology,[19] but the extraction of the EFG parameters from the dephasing curves is not straightforward.

A recently introduced pulse sequence for ultra-wideline NMR has made dramatic improvements in terms of both excitation bandwidth and sensitivity. WURST-QCPMG[20] combines the broadband excitation and refocusing capabilities[21] of frequency-swept wideband, uniform rate, smooth truncation (WURST) pulses[22] with the signal enhancement of the quadrupolar Carr−Purcell−Meiboom−Gill (QCPMG) protocol.[23] The latter protocol involves a repeating loop containing a refocusing pulse and acquisition window, such that the spin−echo can be recorded many times in each scan (over the full time scale of the transverse relaxation). This experiment has been shown to be the most efficient method available for recording broad central-transition powder patterns from half-integer spin quadrupolar nuclei such as ^{35}Cl, ^{65}Cu, ^{71}Ga, or ^{91}Zr, and it works just as well on integer spin nuclei such as ^{10}B.[24,25] When this pulse sequence is applied to ^{14}N nuclei with $C_Q \lesssim 1$ MHz, an additional signal enhancement mechanism resulting from the transfer of Zeeman polarization between the two single-quantum transitions can be exploited, an effect given the name direct enhancement of integer spin magnetization (DEISM).[26] This approach allowed the acquisition of static ^{14}N powder patterns from various crystalline amino acids[27] at a moderate magnetic field strength (9.4 T) in much shorter experimental times than those required for a similar study using MAS.[13] While ^{15}N NMR (on isotopically enriched samples) remains the easiest way to extract isotropic shifts and CSA parameters, the ^{14}N WURST-QCPMG approach has the advantage of allowing fast and accurate characterization of the EFG tensor and (as we will show) is essentially unlimited in terms of the size of the C_Q that can be measured. The EFG tensor is extremely sensitive to the local electronic environment, particularly intermolecular interactions such as hydrogen bonding; thus, this technique can potentially provide important insight into the local structure at the nitrogen site. It has also very recently been shown that ultra-wide-line ^{14}N powder patterns are sensitive to molecular dynamics which modulate the EFG tensor on a time scale similar to C_Q^{-1}.[28]

Herein, we describe the use of the WURST-QCPMG pulse sequence at 21.1 T to characterize the ^{14}N EFG tensors in a variety of common structural motifs of nitrogen. Various model organic and inorganic compounds with C_Q values of up to 4 MHz are studied. While spectral overlap remains an important problem for samples featuring multiple nitrogen sites, we will show that it is possible to distinguish sites with very similar EFG tensor parameters by this method. It is also shown that structural dynamics and relaxation anisotropy can play a crucial role in determining the nature of the ^{14}N spectrum. We further develop the potential of ultra-wideline ^{14}N NMR as a probe of motional processes in solids by showing that local dynamics can affect the ^{14}N line shape via orientational dependencies of N−H dipolar couplings, even when the EFG tensor remains unaltered. Variations in relaxation between different nitrogen environments can also be exploited by the QCPMG protocol to provide a means to preferentially select sites with slower relaxation rates.

We have also conducted extensive density functional theory (DFT) calculations on these systems using various methodologies in order to (1) test the reliability of such calculations in application to ^{14}N NMR, (2) confirm experimental measurements, (3) probe the nuclear shielding tensors and their orientations relative to the EFGs and the molecular frame, (4) assign interaction parameters and spectral features to crystallographic sites where possible, and (5) rationalize the origin of the EFG tensors in terms of contributions from individual molecular orbitals.

The paper is organized as follows: Section 2 outlines the experimental details, tensor conventions, and computational methods. Section 3 presents the ^{14}N NMR spectra obtained and discusses the results in light of plane-wave DFT calculations, molecular dynamics, and relaxation effects. Section 4 presents

(6) Bloom, M.; LeGros, M. A. *Can. J. Phys.* **1986**, *64*, 1522.
(7) Tycko, R.; Opella, S. J. *J. Chem. Phys.* **1987**, *86*, 1761.
(8) Jakobsen, H. J.; Hove, A. R.; Bildsøe, H.; Skibsted, J.; Brorson, M. *J. Magn. Reson.* **2007**, *185*, 159.
(9) Jeschke, G.; Jansen, M. *Angew. Chem., Int. Ed.* **1998**, *37*, 1282.
(10) Ermolaev, K.; Fung, B. M. *J. Chem. Phys.* **1999**, *110*, 7977.
(11) Jakobsen, H. J.; Bildsøe, H.; Skibsted, J.; Giavani, T. *J. Am. Chem. Soc.* **2001**, *123*, 5098.
(12) Giavani, T.; Bildsøe, H.; Skibsted, J.; Jakobsen, H. J. *Chem. Phys. Lett.* **2003**, *377*, 426.
(13) Giavani, T.; Bildsøe, H.; Skibsted, J.; Jakobsen, H. J. *J. Magn. Reson.* **2004**, *166*, 262.
(14) Whitehouse, B. A.; Ray, J. D.; Royer, D. J. *J. Magn. Reson.* **1969**, *1*, 311–326.
(15) Ramamoorthy, A.; Lee, D.-K.; Santos, J. S.; Henzler-Wildman, K. A. *J. Am. Chem. Soc.* **2008**, *130*, 11023.
(16) Qian, C.; Fu, R.; Gor'kov, P.; Brey, W. W.; Cross, T. A.; Gan, Z. *J. Magn. Reson.* **2009**, *196*, 96.
(17) Hill, E. A.; Yesinowski, J. P. *J. Am. Chem. Soc.* **1996**, *118*, 6798.
(18) Yesinowski, J. P.; Hill, E. A. *Solid State NMR Spectroscopy of Inorganic Materials*; American Chemical Society Symposium Series *717*; American Chemical Society: Washington, DC, 1999; p 358.
(19) Hill, E. A.; Yesinowski, J. P. *J. Chem. Phys.* **1999**, *106*, 8650.
(20) O'Dell, L. A.; Schurko, R. W. *Chem. Phys. Lett.* **2008**, *464*, 97.
(21) Bhattacharyya, R.; Frydman, L. *J. Chem. Phys.* **2007**, *127*, 194503.
(22) Kupče, E.; Freeman, R. *J. Magn. Reson. A* **1995**, *115*, 273.
(23) Larsen, F. H.; Jakobsen, H. J.; Ellis, P. D.; Nielsen, N. C. *J. Phys. Chem. A* **1997**, *101*, 8597.
(24) Tang, J. A.; O'Dell, L. A.; Aguiar, P. M.; Lucier, B. E. G.; Sakellariou, D.; Schurko, R. W. *Chem. Phys. Lett.* **2008**, *466*, 227.
(25) O'Dell, L. A.; Rossini, A. J.; Schurko, R. W. *Chem. Phys. Lett.* **2009**, *468*, 330.
(26) O'Dell, L. A.; Schurko, R. W. *J. Am. Chem. Soc.* **2009**, *131*, 6658.
(27) O'Dell, L. A.; Schurko, R. W. *Phys. Chem. Chem. Phys.* **2009**, *11*, 7069.
(28) O'Dell, L. A.; Ratcliffe, C. I. *Chem. Commun.* **2010**, *46*, 6774.

Table 1. Experimental Parameters Used To Acquire the Low-Frequency Half of the ^{14}N Powder Patterns at 21.1 T

sample	initial frequency offset/kHz	pieces	echoes acquired	scans per piece	recycle delay/s	total acquisition time/h
silicon nitride	−400	5	400	8	400	5.3
1,2-dicyanobenzene	−300	10	120	200	10	5.6
1,3-dicyanobenzene	−400	9	120	200	10	5.0
1,4-dicyanobenzene	−400	9	120	200	10	5.0
hydrazine dihydrochloride	−100	10	100	120	3	1.0
urea-d_4	−400	11	8	400	5	6.1
imidazole	−100	8	80	200	10	4.4
melamine	−400	6	120	80	60	8.0

DFT calculations conducted on single molecules and finite-sized clusters, as well as molecular orbital analyses of the EFG tensors in three of the model systems. Finally, Section 5 summarizes the key conclusions.

2. Experimental Details

2.1. Sample Preparation. Three dicyanobenzene samples (1,2-, 1,3-, and 1,4-), urea-d_4, imidazole, and melamine were purchased from Sigma-Aldrich and used without further purification. The hydrazine dihydrochloride sample (BDH Chemicals) was recrystallized from an aqueous solution acidified with dilute hydrochloric acid. For the silicon nitride sample, an empty 4.0 mm Bruker MAS NMR rotor was used. All samples (excluding the silicon nitride rotor) were finely ground before being packed into 7.0 mm outer-diameter, thin-wall zirconia NMR rotors.

2.2. NMR Experiments and Tensor Conventions. All ^{14}N NMR experiments were carried out at 21.1 T ($\nu_L = 65.03$ MHz) using a Bruker Avance II console and a 7.0 mm HX static probe built in-house (National Ultra-High Field NMR Facility for Solids, Ottawa). The WURST-QCPMG pulse sequence was used with eight-step phase cycling[20,29] and 50 μs WURST-80 pulses swept over a range of 1.0 MHz, resulting in an excitation bandwidth of approximately 850 kHz. The optimum RF power for the WURST pulses was experimentally determined as $\nu_1 \approx 30$ kHz. For samples containing protons, continuous-wave ^{1}H decoupling of $\nu_2 \approx 15$ kHz power was applied for the duration of each scan. The decoupling power was limited by the long acquisition times employed in the WURST-QCPMG experiments (tens of milliseconds), and the protons would not be expected to be fully decoupled in most cases. We have found that more advanced heteronuclear decoupling methods such as TPPM or SPINAL provide very little improvement over CW in these particular experiments (data not shown). Other experimental details specific to each sample are presented in Table 1. For the silicon nitride sample, the 400 s recycle delay was insufficient to allow the spins to fully relax to thermal equilibrium, so a dummy scan was included for each piece. We note that the DEISM signal enhancement mechanism[26] is essentially absent from the spectra reported herein due to the width of the static powder patterns, which vastly exceed the effective bandwidth of the applied WURST pulses. In certain spectra, however, wobble-like distortions near the center may be related to this effect, having been previously observed in both experiment and simulation.[26,27] All spectra and calculated shifts are referenced to neat liquid nitromethane at 0.0 ppm.[30] To obtain chemical shift values referenced to liquid NH_3, 381 ppm should be added to the values reported herein. Spectral processing was carried out using the NUTS software (Acorn NMR). QCPMG trains were split into individual echoes which were co-added prior to Fourier transformation. For experiments denoted as "WURST-echo", only the first echo was processed, and the remaining echoes were discarded. Since the extraction of quadrupolar parameters is dependent on precisely locating spectral discontinuities and shoulders, minimal line-broadening was applied. Absorptive spectra were obtained via a magnitude calculation, and complete spectra were reconstructed from the individual pieces via a skyline projection. We have found that, due to the excitation profile of the WURST pulses being approximately rectangular in shape, rather than sinc-like, co-addition of subspectra can often fail to reproduce the true spectral line shape and can give rise to false spectral features if the frequency step size is not carefully chosen. The use of a skyline projection eliminates this issue, provided that the chosen frequency step size is approximately half the excitation bandwidth or less. Herein, we used a step size of 300 kHz in all cases. Experimental EFG parameters were determined by manually fitting simulated powder patterns to the experimental spectra using the Dmfit software,[31] with the best fits determined by visual inspection.

EFG tensors are defined such that the three principal components are ordered $|V_{33}| \geq |V_{22}| \geq |V_{11}|$. The EFG tensor is traceless, allowing the tensor to be fully described using two quantities: the quadrupolar coupling constant (in MHz), given by $C_Q = eQV_{33}/h$ (where eQ is the quadrupole moment of ^{14}N and h is Planck's constant), and the asymmetry parameter, $\eta_Q = (V_{11} - V_{22})/V_{33}$. Nuclear shielding tensors are defined such that the principal components are ordered $\sigma_{33} \geq \sigma_{22} \geq \sigma_{11}$. The relative orientation of the EFG and shielding tensors is described by three Euler angles, α, β, and γ, which move the EFG principal axis system into coincidence with the shielding tensor principal axis system via a series of three positive rotations: α about V_{33}, followed by β around the new V_{22} direction, and finally γ about the new V_{33} (the $zy'z''$ convention). Experimentally, chemical *shifts*, rather than *shieldings*, are measured. We therefore report the calculated shieldings in the form of a chemical shift tensor with principal components $\delta_{11} \geq \delta_{22} \geq \delta_{33}$. Rather than give the values of these principal components, we use the Herzfeld−Berger (or Maryland) convention[32] and report the isotropic shift $\delta_{iso} = (\delta_{11} + \delta_{22} + \delta_{33})/3$ (in ppm), the span $\Omega = \delta_{11} - \delta_{33}$ (also in ppm), and the skew $\kappa = 3(\delta_{22} - \delta_{iso})/\Omega$ (dimensionless, and ranging from −1.0 to 1.0). Since the calculated isotropic shielding is reported relative to a bare nucleus, the chemical shift of which cannot be measured experimentally, the conversion of calculated shielding parameters to the ^{14}N chemical shift scale was achieved by plotting all calculated isotropic shieldings against experimental isotropic shift values (from the literature) to obtain the linear relationship between them. This plot is shown in Figure 1a and discussed further in section 3.1. Euler angles were determined using EFGShield.[33] It is worth noting here that the Euler angle β always describes the angle between the largest EFG component V_{33} and the most shielded component of the CS tensor (σ_{33}, or equivalently δ_{33}). When $\beta = 0$, the angle between V_{22} and δ_{22}/σ_{22} is given by the sum of α and γ.

For each sample, only the low-frequency half of the ^{14}N NMR spectrum was acquired, and the remaining half was reconstructed from this by reflection about the isotropic shift value (obtained either from the literature or from DFT calculations). For samples featuring multiple sites, the average of the isotropic shifts was used as the point of reflection. The low-frequency half of the spectrum was chosen for acquisition simply because the tuning range of the probe happened to extend further in that direction. The justification for this strategy is that second-order quadrupolar or CSA effects, which cause departure from symmetry, are of the order of a few tens of kHz in size, which is negligible compared with the widths of the ultra-wideline powder patterns that we present and smaller than the experimental uncertainties in our reported C_Q values. A more quantitative justification is given

(29) Hung, I.; Gan, Z. *J. Magn. Reson.* **2010**, *204*, 256.
(30) Harris, R. K.; Becker, E. D.; Cabral de Menezes, S. M.; Goodfellow, R.; Granger, P. *Pure Appl. Chem.* **2001**, *73*, 1795.
(31) Massiot, D.; Fayon, F.; Capron, M.; King, I.; Le Calvé, S.; Alonso, B.; Durand, J. O.; Bujoli, B.; Gan, Z.; Hoatson, G. *Magn. Reson. Chem.* **2002**, *40*, 70.
(32) Mason, J. *Solid State Nucl. Magn. Reson.* **1993**, *2*, 285.
(33) Adiga, S.; Aebi, D.; Bryce, D. L. *Can. J. Chem.* **2007**, *85*, 496.
(34) Bak, M.; Rasmussen, J. T.; Nielsen, N. C. *J. Magn. Reson.* **2000**, *147*, 296.

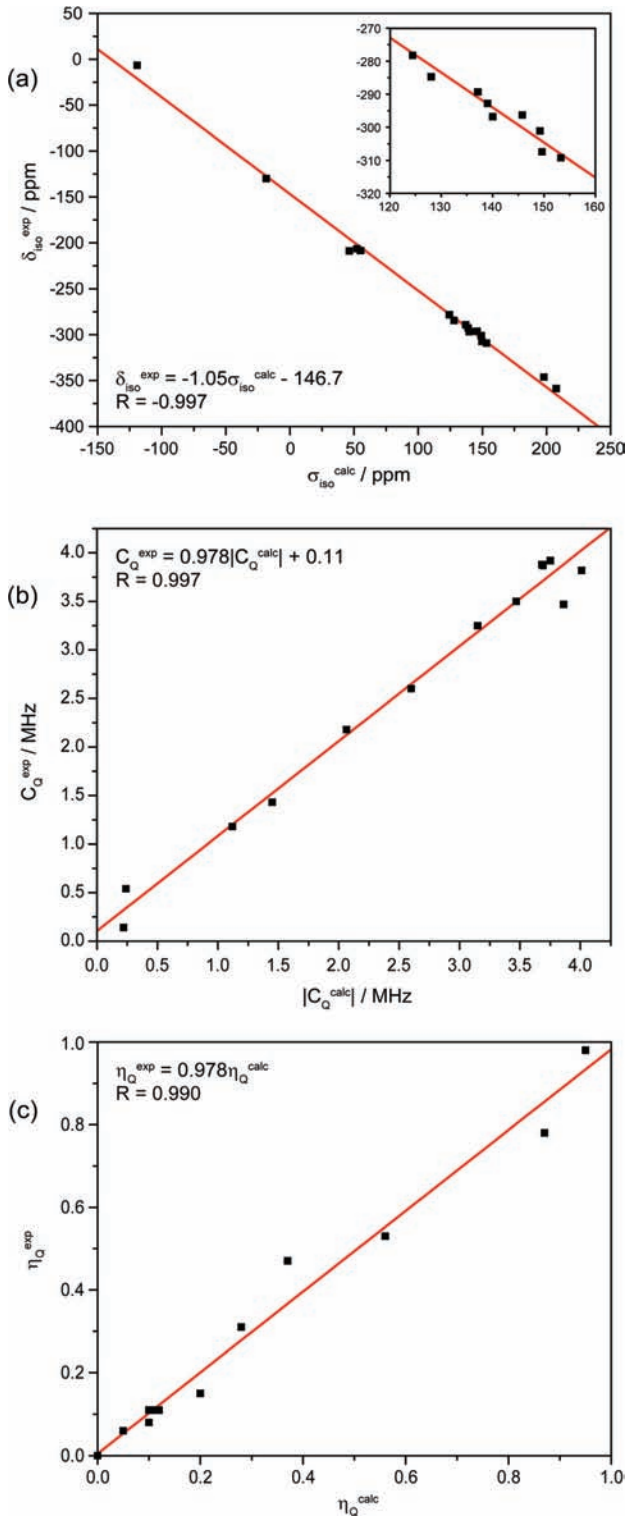

Figure 1. Plots of experimental ^{14}N NMR parameters (from this study as well as from the literature) against plane-wave DFT calculations. (a) Experimental isotropic chemical shifts versus calculated isotropic shieldings (expansion shown inset), (b) quadrupolar coupling constants, and (c) quadrupolar asymmetry parameters.

in the Supporting Information. Finally, we reiterate that, while the above strategy is advantageous for a determination of the ^{14}N EFG parameters, nitrogen isotropic shifts and CS tensors are more easily studied using alternative techniques, ideally ^{15}N NMR spectroscopy of isotopically enriched samples.

2.3. Simulations of ^{14}N NMR Line Shapes in the Presence of Dynamics. The EXPRESS software[35] was used within MATLAB 7.10 to simulate the effects of dynamics on the ^{14}N NMR spectra of urea[28] and imidazole. Dynamics were modeled as Markovian jump processes at specified jump rates between different EFG tensor orientations determined from DFT calculations and defined using Euler angles and the parameters outlined above. The effects of the CS tensor were neglected. A simulation of the full WURST-QCPMG sequence would be highly computationally demanding due to the phase-modulated nature of the WURST pulses, the long acquisition period, and the large number of crystallite orientations over which the simulations must be averaged. The experiment was therefore modeled as a two-pulse quadrupolar echo sequence with rectangular, monochromatic pulses separated by a variable echo delay. The validity of this model has yet to be fully tested, though it has been used previously to obtain jump rates for the molecular flipping mechanism in urea that were in good agreement with those obtained by other, more established techniques.[28] Powder averaging was conducted over a minimum of 75 000 crystal orientations calculated using the ZCW method, with longer echo delays requiring more orientations to achieve line shape convergence. Simulations took up to several hours to run on a Windows PC, depending primarily on the size of the echo delay used. Simulated FIDs were processed within EXPRESS by shifting to the echo top, with 20−50 Hz exponential apodization applied before Fourier transformation.

2.4. DFT Calculations. Plane-wave DFT calculations were performed using the CASTEP software[36−39] in the Materials Studio 4.3 software suite. This software employs the gauge-including projector-augmented wave algorithm (GIPAW).[36] Revised Perdew, Burke, and Ernzerhof (RPBE) functionals were used with the generalized gradient approximation for the exchange-correlation energy. Plane wave basis set cut-offs and Monkhorst−Pack *k*-space grid sizes were set automatically under a "fine" basis set accuracy (see Supporting Information for specific values). Where appropriate, proton positions were optimized using a Broyden−Fletcher−Goldfarb−Shanno optimization algorithm,[40] with the lattice parameters and coordinates of all other atoms fixed. Ultrasoft ^{14}N pseudopotentials were used for the EFG calculations.[38] The crystal structures used in the CASTEP calculations were obtained from the following references: silicon nitride,[41] 1,2-dicyanobenzene,[42] 1,3-dicyanobenzene,[43] 1,4-dicyanobenzene,[44] hydrazine dihydrochloride,[45] urea,[46] imidazole,[47] melamine,[48] α-glycine,[49] lead nitrate,[50] cubic boron nitride,[51] and hexagonal boron nitride.[51]

DFT calculations of EFG tensors in molecules and finite-size clusters were carried out using revision 2009.01 and a 2010 developer's version of the Amsterdam Density Functional (ADF)

(35) Vold, R. L.; Hoatson, G. L. *J. Magn. Reson.* **2009**, *198*, 57.
(36) Clark, S. J.; Segall, M. D.; Pickard, C. J.; Hasnip, P. J.; Probert, M. J.; Refson, K.; Payne, M. C. *Z. Kristallogr.* **2005**, *220*, 567.
(37) Pickard, C. J.; Mauri, F. *Phys. Rev. B* **2001**, *63*, 245101.
(38) Profeta, M.; Mauri, F.; Pickard, C. J. *J. Am. Chem. Soc.* **2003**, *125*, 541.
(39) Yates, J. R.; Pickard, C. J.; Mauri, F. *Phys. Rev. B* **2007**, *76*, 024401.
(40) Pfrommer, B. G.; Cote, M.; Louie, S. G.; Cohen, M. L. *J. Comput. Phys.* **1997**, *131*, 233.
(41) Kohatsu, I.; McCauley, J. W. *Mater. Res. Bull.* **1974**, *9*, 917.
(42) Janczak, J.; Kubiak, R. *Acta Crystallogr. C* **1995**, *51*, 1399.
(43) Janczak, J.; Kubiak, R. *J. Mol. Struct.* **2000**, *553*, 157.
(44) Guth, H.; Heger, G.; Drueck, U. *Z. Kristallogr.* **1982**, *159*, 185.
(45) Kruszynski, R.; Trzesowska, A. *Acta Crystallogr. E* **2007**, *63*, 179.
(46) Guth, H.; Heger, G.; Klein, S.; Treutmann, W.; Scheringer, C. *Z. Kristallogr.* **1980**, *153*, 237.
(47) Craven, B. M.; McMullan, R. K.; Bell, J. D.; Freeman, H. C. *Acta Crystallogr. B* **1977**, *33*, 2585.
(48) Varghese, J. N.; O'Connell, A. M.; Maslen, E. N. *Acta Crystallogr. B* **1977**, *33*, 2102.
(49) Power, L. F.; Turner, K. E.; Moore, F. H. *Acta Crystallogr. B* **1976**, *32*, 11.
(50) Nowotny, H.; Heger, G. *Acta Crystallogr. C* **1986**, *42*, 133.
(51) Wyckoff, R. W. G. *Crystal Structures*, 2nd ed.; Interscience: New York, 1963; p 85.

code.[52−54] The density functional was composed of the PW92[55] local density approximation along with the PBE[56] exchange and correlation terms. Slater-type basis sets of triple-zeta, doubly polarized quality in the valence region were used for all calculations. Prior to calculation of EFG tensors for all isolated and cluster models, proton positions in diffraction-derived model structures were optimized as described above. A locally modified version of the NBO 5.0 code[57] was used to generate natural localized molecular orbitals (NLMOs), natural bond orbitals (NBOs), and analysis data for EFGs based on these orbital sets. The modifications of NBO include the use an OpenMP parallelization and the use of efficient BLAS routines, allowing the treatment of systems with several thousand basis functions.

3. Results and Discussion

3.1. Reliability of Plane-wave DFT Calculations. Prior to a discussion of the experimental results for each individual sample, it is useful to briefly consider the overall performance of the plane-wave DFT calculations made using CASTEP. All experimental and calculated results are presented in Table 2. As well as the various model compounds for which the ^{14}N NMR spectra were collected, calculations were also run on α-glycine, lead nitrate, and boron nitride (both cubic and hexagonal phases) in order to provide a broader range of interaction parameters over which to compare the experimental and calculated results (^{14}N NMR parameters for these systems have been published previously).[9,11,12,27,58] The computational results for the three most commonly reported ^{14}N NMR parameters (δ_{iso}, C_Q, and η_Q) are plotted in Figure 1 against the experimental values (similar plots were not made for the other parameters due to a paucity of experimental data). For the isotropic shifts (Figure 1a), a linear fit resulted in both a correlation coefficient and slope very close to −1.0 (the negative sign arising due to the inverse relationship between nuclear magnetic shielding and chemical shift values), and excellent agreement is achieved over a range of approximately 350 ppm. This plot was used to determine the isotropic chemical shifts for the dicyanobenzenes and hydrazine dihydrochloride samples, about which the experimental spectra were reflected.

A similar level of agreement was observed for the quadrupolar coupling constants (Figure 1b) across a range of values from 0 to ∼4 MHz. Both the correlation coefficient and slope are very close to 1.0. We note that the two data points corresponding to urea and hydrazine dihydrochloride each show a significant deviation from the line of best fit (top right corner of the plot). One possible reason for this is that both of these samples are known to exhibit dynamic processes which are not accounted for in the calculations. For the remaining systems, the CASTEP calculations underestimate the ^{14}N C_Q values by approximately 100 kHz, a systematic error that can be easily corrected for after the fact. This should be kept in mind when comparing the experimental and calculated C_Q values in Table 2.

The quadrupolar asymmetry parameter η_Q shows a level of agreement between experimental and calculated values similar to that observed for C_Q (Figure 1c), with the correlation coefficient and slope both fairly close to unity. It should be noted that the two calculated values of η_Q showing the largest disagreement with experiment are both from melamine, for which each point represents the average of three distinct crystallographic nitrogen sites that were not well resolved in the experimental spectrum (see section 3.7). The (average) calculated C_Q values for these sites agreed well with experimental values, in contrast to the results for η_Q.

3.2. Silicon Nitride. Favorable thermal and mechanical properties make silicon nitride a useful material for the construction of rotors for MAS NMR, as well as numerous engineering applications. The α-Si_3N_4 crystal structure[41] features four distinct nitrogen environments in a 3:3:1:1 ratio. Each site is coordinated to three silicon atoms, with the two less abundant sites (N3 and N4) existing on three-fold symmetry axes. The β-Si_3N_4 phase[59] features two distinct sites in a 3:1 ratio, also with the less abundant site on a three-fold symmetry axis. Both phases have been previously studied by Harris et al. using ^{15}N MAS NMR on enriched samples,[60] with isotropic chemical shifts reported for all four sites in α-Si_3N_4 (see Table 2) and the authors noting very long spin−lattice relaxation times for ^{15}N (ca. 3000 s). Similarly long relaxation times were also observed in our ^{14}N experiments on a silicon nitride NMR rotor, which would most likely consist of a mixture of both phases, the ratio depending on the exact manufacturing conditions.[61] The effects of long relaxation times on the WURST-QCPMG experiment are twofold: long T_1 values mean that lengthy recycle delays must be used between scans to allow sufficient longitudinal magnetization to be re-established, but long T_2 values allow a very large number of echoes to be acquired, thereby boosting the signal obtained from each individual scan. In this instance, the long recycle delay (set arbitrarily at 400 s with the addition of a dummy scan) resulted in a ^{14}N NMR spectrum of relatively poor S/N ratio compared with other spectra obtained in a similar time frame (Figure 2), despite the acquisition of 400 echoes in each scan. The spectrum was fitted using a single line shape with quadrupolar parameters $C_Q = 2.18$ MHz and $\eta_Q = 0.08$, values close to those predicted by plane-wave DFT for sites N1 and N2 in the α-Si_3N_4 structure. The overall quality of this spectrum is comparable to that reported by Yesinowski and Hill, who were able to use recycle delays much shorter than T_1 by continuously changing the observed nuclei with slow mechanical rotation of the sample (RotIsseRIe).[17] The N3 and N4 sites are predicted to have $\eta_Q = 0.00$ due to their three-fold symmetry; thus, their ^{14}N powder patterns should have relatively sharp discontinuities that are separated due to their different C_Q values. However, such features are not visible in this experimental spectrum. We also note that the presence of β-Si_3N_4, which has very similar nitrogen environments, will further complicate the spectrum. In order to resolve these sites in a quantitative fashion, a much longer recycle delay

(52) te Velde, G.; Bickelhaupt, F. M.; van Gisbergen, S. J. A.; Fonseca Guerra, C.; Baerends, E. J.; Snijders, J. G.; Ziegler, T. *J. Comput. Chem.* **2001**, *22*, 931.
(53) Fonseca Guerra, C.; Snijders, J. G.; te Velde, G.; Baerends, E. J. *Theor. Chem. Acc.* **1998**, *99*, 391.
(54) *ADF2009.01*, SCM, Theoretical Chemistry; Vrije Universiteit, Amsterdam, The Netherlands, http://www.scm.com.
(55) Perdew, J. P.; Wang, Y. *Phys. Rev. B* **1992**, *45*, 13244.
(56) Perdew, J. P.; Burke, K.; Ernzerhof, M. *Phys. Rev. Lett.* **1996**, *77*, 3865.
(57) Glendening, E. D.; Badenhoop, J. K.; Reed, A. E.; Carpenter, J. E.; Bohmann, J. A.; Morales, C. M.; Weinhold, F. *NBO*, 5.0; Theoretical Chemistry Institute, University of Wisconsin: Madison, WI, 2009; http://www.chem.wisc.edu/ nbo5.
(58) Strohmeier, M.; Stueber, D.; Grant, D. M. *J. Phys. Chem. A* **2003**, *107*, 7629.
(59) Grün, R. *Acta Crystallogr. B* **1979**, *35*, 800.
(60) Harris, R. K.; Leach, M. J.; Thompson, D. P. *Chem. Mater.* **1990**, *2*, 320.
(61) Lange, H.; Wötting, G.; Winter, G. *Angew. Chem., Int. Ed. Engl.* **1991**, *30*, 1579.

Table 2. Experimental and Calculated Tensor Parameters and Euler Angles[a]

		EFG tensor		chemical shift tensor			Euler angles		
sample	site	C_Q/MHz	η_Q	δ_{iso}/ppm	Ω/ppm	κ	α	β	γ
silicon nitride	N1	−2.12	0.06	−303.8	14.7	0.73	191	28	234
		2.18[c]	**0.08**[c]	**−307.4**[d]					
	N2	−2.01	0.14	−307.7	31.8	−0.14	266	20	228
		2.18[c]	**0.08**[c]	**−309.2**[d]					
	N3	−1.67	0.00	−281.1	6.9	1.00	60	3	55
				−284.7[d]					
	N4	−2.54	0.00	−293.7	33.3	1.00	60	1	271
				−296.8[d]					
1,2-dicyanobenzene	N1	−3.75 (−4.11)	0.12 (0.08)	−90.9 (−104.7)	406.2 (405.8)	0.86 (0.89)	109 (207)	0 (0)	256 (157)
		3.92	**0.11**						
1,3-dicyanobenzene	N1	−3.69 (−4.09)	0.10 (0.07)	−98.8 (−111.3)	406.7 (408.4)	0.90 (0.92)	143 (132)	0 (0)	212 (223)
		3.88[c]	**0.11**[c]						
	N2	−3.68 (−4.16)	0.11 (0.08)	−97.1 (−113.1)	401.7 (398.4)	0.88 (0.90)	40 (24)	0 (0)	320 (336)
		3.88[c]	**0.11**[c]						
1,4-dicyanobenzene	N1	−3.69 (4.02)	0.05 (0.04)	−93.6 (−109.9)	392.9 (395.0)	0.93 (0.95)	72 (72)	0 (0)	279 (278)
		3.87	**0.06**						
hydrazine dihydrochloride	N1	4.01 (4.87)	0.00 (0.00)	−313.0 (−366.5)	30.1 (52.6)	1.00 (1.00)	324 (0)	0 (0)	180 (0)
		3.82	**0.00**						
urea-d_4	N1	−3.86 (−3.81)	0.28 (0.22)	−303.4 (−313.2)	125.7 (120.5)	−0.15 (−0.02)	85 (84)	90 (90)	270 (90)
		3.47	**0.31**	**−301.1**[e]					
imidazole	N1	1.45 (−1.39)	0.95 (0.92)	−195.3 (−207.9)	226.9 (219.5)	0.43 (0.38)	93 (1)	90 (2)	252 (17)
		1.43	**0.98**	**−209.0**[f]	**201.8**[f]	**0.43**[f]			
	N2	−3.15 (−3.28)	0.20 (0.10)	−127.3 (−137.6)	402.0 (403.1)	0.51 (0.51)	181 (181)	89 (89)	276 (275)
		3.25	**0.15**	**−130.0**[f]	**379.1**[f]	**0.57**[f]			
melamine	N1	−3.34 (−3.38)	0.35 (0.31)	−290.7 (−293.6)	104.4 (109.6)	−0.69 (−0.58)	268 (267)	84 (85)	94 (94)
		3.50[g]	**0.47**[g]	**−289.3**[i]					
	N2	−3.53 (−3.57)	0.35 (0.31)	−292.7 (−298.5)	110.6 (111.7)	−0.46 (−0.38)	68 (67)	90 (88)	270 (271)
		3.50[g]	**0.47**[g]	**−292.8**[i]					
	N3	−3.54 (−3.55)	0.31 (0.27)	−299.8 (−304.4)	102.2 (102.5)	−0.15 (−0.12)	288 (285)	80 (80)	91 (270)
		3.50[g]	**0.47**[g]	**−296.3**[i]					
	N4	2.60 (2.56)	0.93 (0.99)	−201.6 (−209.5)	274.4 (270.4)	0.76 (0.76)	178 (178)	88 (88)	172 (173)
		2.60[h]	**0.78**[h]	**−206.5**[i]					
	N5	2.58 (2.53)	0.79 (0.86)	−204.5 (−210.7)	260.1 (258.8)	0.77 (0.78)	182 (181)	89 (89)	187 (186)
		2.60[h]	**0.78**[h]	**−208.6**[i]					
	N6	2.63 (2.57)	0.90 (0.95)	−204.7 (−211.0)	265.2 (262.9)	0.72 (0.73)	3 (2)	90 (89)	184 (184)
		2.60[h]	**0.78**[h]	**−208.6**[i]					
glycine[b]	N1	1.12	0.56	−354.6	14.4	−0.67	285	77	90
		1.18[j]	**0.53**[j]	**−346.3**[k]	**17.8**[k]	**0.05**[k]			
lead nitrate[b]	N1	−0.24	0.00	−21.5	186.0	1.00	0	0	0
		0.54[l]	**0.00**[l]	**−6.7**[m]	**156.7**[m]	**−0.77**[m]			
boron nitride (cubic)[b]	N1	0.00	−	−364.7	0.0				
				−358.8[n]					
boron nitride (hexagonal)[b]	N1	−0.22	0.00	−277.3	216.4	0.99	30	0	0
		0.14[n]		**−278.2**[n]					

[a] Calculated values are shown in regular type, and experimentally determined values are shown in boldface. Uncertainties in the reported experimental C_Q and η_Q parameters are unique to each value and are not shown but are generally in the region of ±0.05 MHz for C_Q and ±0.05 for η_Q. Site numbers correspond to crystal structures used (see text). Parentheses indicate quantities calculated from non-optimized structures, adjacent values having been calculated using optimized proton/deuteron positions. Experimental C_Q values give only the absolute values, while calculated values also give the sign. Calculated chemical shifts were derived from isotropic shielding values using the expression given in Figure 1a. The Euler angles describe the orientation of the EFG tensor relative to the chemical shift tensor. [b] NMR spectra not presented. [c] Average of sites N1 and N2. [d] Reference 60. [e] Reference 72. [f] Reference 80. [g] Average of sites N1, N2, and N3. [h] Average of sites N4, N5, and N6. [i] Reference 96. [j] Reference 27. [k] Reference 58. [l] Reference 11. [m] Reference 12. [n] Reference 9.

would be required to allow for full spin−lattice relaxation, in addition to a greater number of scans to improve the S/N ratio. Due to time limitations, this was not attempted.

The isotropic chemical shifts for the four sites in α-Si_3N_4 calculated using CASTEP each fall within ca. 4 ppm of the experimental values obtained in the ^{15}N study.[60] The close proximity of the experimental shifts reported for the N1 and N2 sites (1.8 ppm difference) means that the assignment of the parameters to those sites in Table 2 is only tentative, but for the N3 and N4 sites the assignment is more convincing. Both the calculated EFG and CS tensors for the N3 and N4 sites are axially symmetric, with the unique components (V_{33}

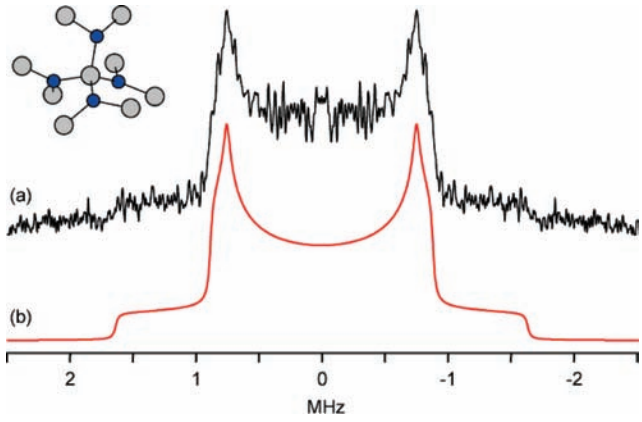

Figure 2. (a) Experimental ^{14}N NMR spectrum of an empty silicon nitride MAS NMR rotor. (b) Fitted simulation made using parameters $C_Q = 2.18$ MHz and $\eta_Q = 0.08$. Inset: A fragment of the crystal structure showing the three-fold coordination of nitrogen with silicon (nitrogen atoms in blue).

and σ_{33}) coincident and oriented parallel to the axis of three-fold symmetry. For both the N1 and N2 sites, V_{33} is perpendicular to the plane made by the three neighboring silicon atoms, while σ_{33} is tilted away from V_{33} by 28° and 20°, respectively.

3.3. Dicyanobenzenes. Despite their increased width, the ^{14}N powder patterns obtained from the three dicyanobenzene samples (Figure 3) show a dramatic improvement in S/N ratio over the silicon nitride spectrum acquired in a similar amount of time (ca. 5 h). This is due to the increased spin−lattice relaxation rate of the ^{14}N nuclei in the dicyanobenzenes, which allowed much shorter recycle delays and hence more scans per unit time, while the transverse (spin−spin) relaxation rates are still slow enough to permit the acquisition of a large number of echoes in each scan. Such conditions are perfectly suited for QCPMG-type experiments, hence the high S/N ratios of the spectra in Figure 3. The increased spin−lattice relaxation efficiency in these samples relative to Si_3N_4 can be attributed to at least two factors: (1) the less rigid lattice and presence of librational motions, and (2) the presence of protons and concomitant fluctuating N−H dipolar couplings. The reduced intensity at the center of the spectrum of the 1,2-dicyanobenzene (Figure 3a) is due to the transmitter frequency for the first piece acquired being set closer to the isotropic shift (300 kHz offset), resulting in distortions similar to those observed in DEISM simulations published previously.[26,27] Subsequently, a 400 kHz offset was found to be sufficient to minimize this distortion while still adequately exciting the central region of the patterns (see other spectra). All three spectra were fitted with single ^{14}N powder patterns to obtain the quadrupolar parameters reported in Table 2. 1,3-Dicyanobenzene, however, has two distinct crystallographic nitrogen sites, for which plane-wave DFT predicts very similar values for the EFG and CS tensor parameters. In fact, these two sites *can* be distinguished experimentally if the spectra are recorded using a higher resolution (i.e., a larger number of data points acquired for each echo, which also has the effect of reducing the overall S/N ratio since fewer echoes can be acquired overall). Five out of the six spectral features from the low-frequency half of the spectrum can be resolved in this way (Figure 4). The outermost region of the pattern appears as a single shoulder (Figure 4c), indicating that the two sites have almost identical C_Q values but differ slightly in η_Q, as the latter parameter has no effect on the position of the outermost shoulder (a similar effect was also

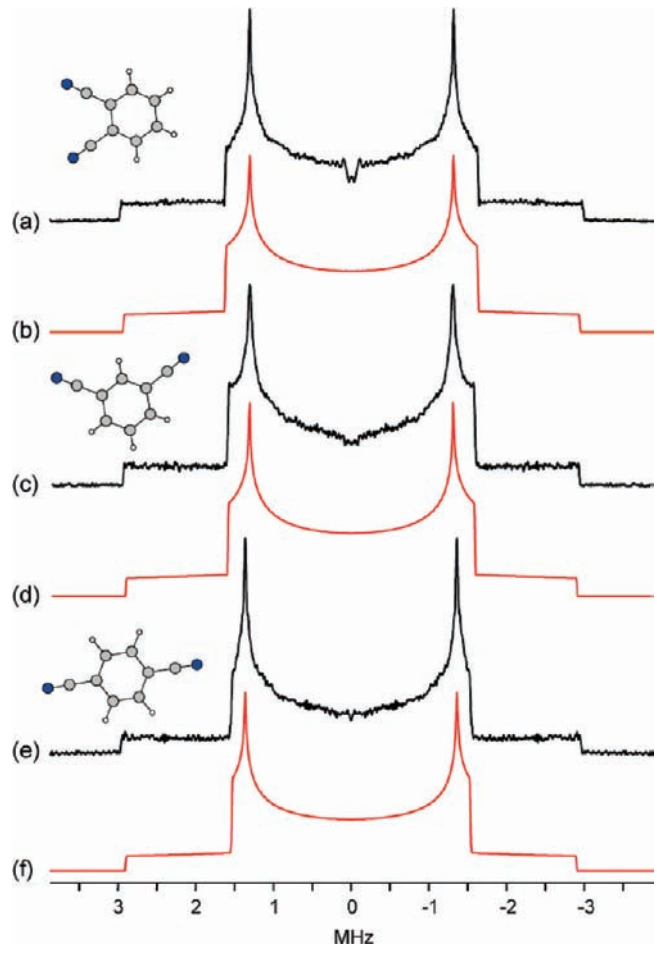

Figure 3. Experimental ^{14}N NMR spectra of (a) 1,2-dicyanobenzene, (c) 1,3-dicyanobenzene, and (e) 1,4-dicyanobenzene, with fitted simulations shown in (b), (d), and (f), respectively. The molecular structures are shown inset next to each spectrum (nitrogen atoms in blue, carbons in gray).

observed in the static ^{14}N NMR spectrum of L-leucine).[27] While the frequency separation of the resolved features in Figure 4a,b is similar in magnitude to the possible effects of CSA or second-order QI discussed in the Supporting Information, both sites in this case are predicted by plane-wave DFT to have very similar EFG and CS tensor parameters and orientations. A simulation of the two full sets of calculated interaction parameters, including first- and second-order QI and CSA (Figure 4d), shows differences in the positions of the spectral features that are in reasonable agreement with the experimental spectra, and the experimental features have therefore been tentatively assigned on the basis of this simulation. This serves as an example of how the ultra-wideline nature of ^{14}N powder patterns can be considered as an advantage in certain instances because the dispersion of spectral features across a wide frequency range can allow small differences in interaction parameters to be resolved (provided, of course, that a sufficient S/N ratio can be obtained).

After an optimization of the proton positions, the quadrupolar parameters predicted by plane-wave DFT are in good agreement with the experimental values for all three dicyanobenzene samples (see Table 2). Both the calculated EFG and shielding tensors are fairly close to axially symmetric, and the V_{33} and σ_{33} components are coincident and parallel to the C≡N bond (to within 1°) in all cases, as would be expected. The calculated orientation of V_{22} is within 2° of the plane of the molecule for

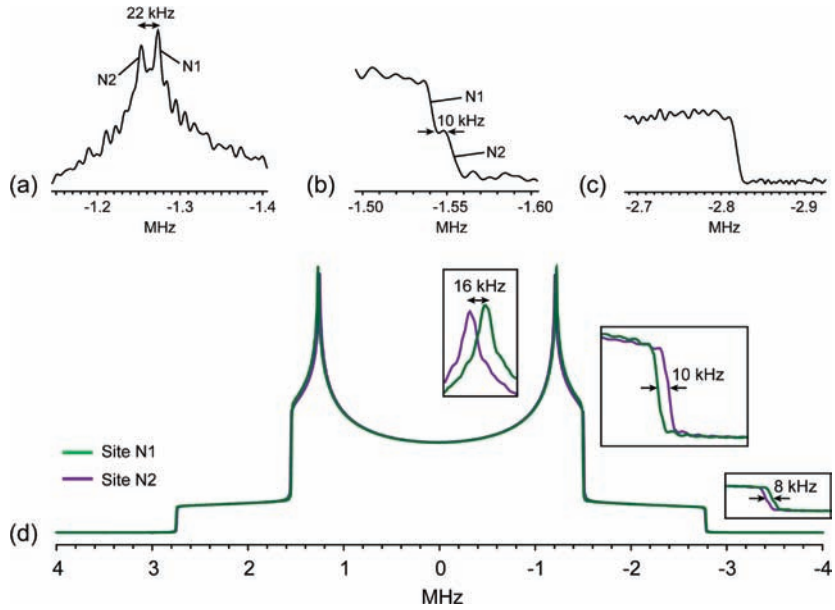

Figure 4. (a−c) High-resolution experimental pieces of the 1,3-dicyanobenzene spectrum. (d) Simulation of all interaction parameters as predicted by CASTEP (see Table 2) with expansions around certain spectral features shown inset. Assignments of spectral features are made in (a) and (b) based on the simulation.

each site, except for that of 1,4-dicyanobenzene, for which it is tilted at an angle of ca. 9° relative to the plane of the benzene ring. This is a result of intermolecular effects and is discussed further in section 4.1.

3.4. Hydrazine Dihydrochloride. A fragment of the hydrazine dihydrochloride structure is shown as an inset in Figure 5. The single unique nitrogen environment is axially symmetric (C_3 symmetry), and, as one would expect, this is reflected in axially symmetric EFG and CS tensors predicted by plane-wave DFT (see Table 2), with V_{33} and σ_{33} coincident. Note that since $V_{11} = V_{22}$ and $\sigma_{11} = \sigma_{22}$, the values of the Euler angles α and γ are essentially meaningless in this instance. While this symmetry fixes the value of η_Q to zero, the calculated C_Q value for this sample is overestimated, even after optimization of the proton positions (see Figure 1b). This may be due to the dynamics of the $N_2H_6^{2-}$ ion. Primarily, this consists of a rotation of the NH_3 groups around the N−N bond axis, a process that has been characterized by ^{1}H solid-state NMR relaxation[62] as well as other techniques.[63,64] This motion in itself would not alter the ^{14}N C_Q, though other modes are possible which could alter the experimentally measured C_Q. For example, the C_Q could potentially be altered by librational motion of the protons, resulting in their average positions being different from that specified in the crystal structure used for the calculation. Nonetheless, the WURST-echo spectrum shows excellent agreement with the fitted simulation in Figure 5b, allowing an accurate measurement of the C_Q value as 3.82 MHz.

Significant anisotropy in the QCPMG enhancement is clearly visible in the WURST-QCPMG spectra in Figure 5c, with increased signal intensity near the center of the pattern (especially visible in the non-decoupled spectrum) arising from a greater number of echoes being acquired in the QCPMG train. This anisotropy is caused by the rotational dynamics of the NH_3 groups. The center of the pattern corresponds to crystallites oriented with the NH_3 rotation axis at $\theta = 54.7°$ (the magic angle) relative to the external magnetic field. Thus, this rotation will decouple the N−H dipolar interactions and reduce their contribution to the dephasing of the ^{14}N magnetization in this region. Further out from the center of the pattern, the NH_3 rotation fails to average out the dipolar couplings and will even enhance the ^{14}N relaxation for components of the rotation that occur at rates comparable to the ^{14}N Larmor frequency. Increasing the strength of the proton decoupling reduces dephasing due to N−H dipolar couplings for *all* orientations; thus, the spectrum approaches the ideal shape. The small dip in the very center of the pattern is likely due to distortions related to the DEISM effect mentioned previously.[26,27] A complete picture of the dephasing/relaxation effects in this system would require an additional consideration of the effects of H−H dipolar couplings, but this is beyond the scope of this article.

We have therefore shown that ultra-wideline ^{14}N NMR line shapes can be sensitive to local dynamics, even when those dynamics cause no change in the magnitude or orientation of the EFG tensor. In this case, the dynamics affect the shape of the powder pattern via the orientation dependence of N−H dipolar couplings, which result in anisotropy observable as a variation in QCPMG enhancement. We note that relaxation caused by the modulation of N−H dipolar couplings has recently been illustrated in solid-state ^{15}N NMR experiments conducted on proteins and was used to extract quantitative dynamic information.[65−67] We are currently using ^{14}N NMR to study other hydrazine systems, and a more detailed investigation into the mechanisms at play in such systems will be the subject of a future publication.

(62) Ratcliffe, C. I. *J. Magn. Reson.* **1980**, *38*, 283.
(63) Ludman, C. J.; Ratcliffe, C. I.; Waddington, T. C. *J. Chem. Soc. Faraday Trans.* **1976**, *72*, 1741.
(64) Ratcliffe, C. I.; Sherman, W. F.; Wilkinson, G. R. *J. Raman. Spectrosc.* **1981**, *11*, 199.
(65) Giraud, N.; Böckmann, A.; Lesage, A.; Penin, F.; Blackledge, M.; Emsley, L. *J. Am. Chem. Soc.* **2004**, *126*, 11422.
(66) Giraud, N.; Blackledge, M.; Goldman, M.; Böckmann, A.; Lesage, A.; Penin, F.; Emsley, L. *J. Am. Chem. Soc.* **2005**, *127*, 18190.
(67) Giraud, N.; Sein, J.; Pintacuda, G.; Böckmann, A.; Lesage, A.; Blackledge, M.; Emsley, L. *J. Am. Chem. Soc.* **2006**, *128*, 12398.

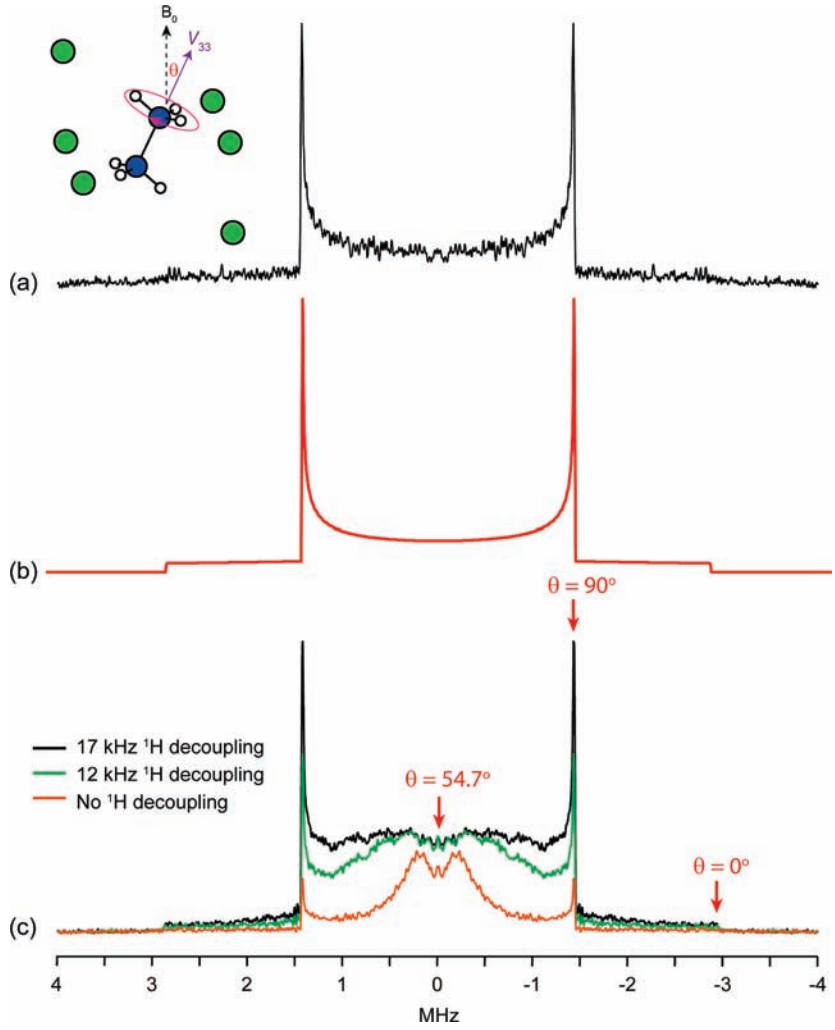

Figure 5. (a) Experimental WURST-echo spectrum obtained from the hydrazine dihydrochloride sample, (b) a fitted simulation made using parameters C_Q = 3.82 MHz and η_Q = 0.00, and (c) WURST-QCPMG spectra obtained with different proton decoupling strengths as shown. A fragment of the crystal structure is shown inset (nitrogen atoms in blue, chlorines in green). The angle between the N−N vector (which is coincident with V_{33}) and the external magnetic field B_0 is labeled as θ.

3.5. Urea-d_4. An undeuterated sample of urea, initially studied at 9.4 T, was found to have a very short transverse relaxation time for the ^{14}N nuclei (as measured via the WURST-QCPMG echo train), which drastically reduces the number of echoes that can be acquired. A deuterated sample was therefore obtained in the hope of increasing the T_2, since the deuteration of a sample of L-leucine was found to increase the ^{14}N T_2 significantly in a previous study,[27] allowing for a greater QCPMG enhancement. Unfortunately, the apparent T_2 in the urea-d_4 sample is still relatively short (ca. 0.25 ms at 21.1 T), allowing only eight echoes to be acquired before the transverse magnetization is lost completely. This relatively fast relaxation was subsequently found to be due to the dynamics present in this system. Urea molecules in the crystal undergo two types of motion: 180° flipping of the molecule around the carbonyl bond axis, and rotation of the amine groups around the N−C bonds. These two dynamic processes have been studied previously by ^{1}H NMR,[68,69] ^{2}H NMR,[70−72] and ^{14}N NQR.[73−76] The former motion is known to occur at ambient temperatures, and we have very recently shown that it can be studied in a quantitative fashion using ^{14}N ultra-wideline NMR.[28] We refer the reader to this reference for more details, but here we provide a very brief recap prior to further discussion of the ^{14}N EFG tensor in urea in section 4.2.

The ^{14}N WURST-echo spectrum in Figure 6a was fitted to obtain EFG parameters of C_Q = 3.47 MHz and η_Q = 0.31. While some previous studies have assumed the V_{33} component of the ^{14}N EFG tensor in urea to be parallel to the N−C bond,[70,76] our CASTEP calculations predict it to be perpendicular to the molecular plane, with V_{22} within 2° of the N−C bond (the σ_{33} component of the shielding tensor is also aligned almost parallel to the N−C bond, with σ_{22} perpendicular to the molecular plane). As with the hydrazine dihydrochloride system discussed above, the C_Q value predicted by plane-wave DFT values is overestimated (Table 2 and Figure 1), and once again this may be due

(68) Kromhout, R. A.; Moulton, W. G. *J. Chem. Phys.* **1955**, *23*, 1673.
(69) Emsley, J. W.; Smith, J. A. S. *Trans. Faraday Soc.* **1961**, *57*, 1233.
(70) Chiba, T. *Bull. Chem. Soc. Jpn.* **1965**, *38*, 259.
(71) Williams, J. C.; McDermott, A. E. *J. Phys. Chem.* **1993**, *97*, 12393.
(72) Taylor, R. E.; Bacher, A. D.; Dybowski, C. *J. Mol. Struct.* **2007**, *846*, 147.
(73) Chiba, T.; Toyama, M.; Morino, Y. *J. Phys. Soc. Jpn.* **1959**, *14*, 379.
(74) Minematsu, M. *J. Phys. Soc. Jpn.* **1959**, *14*, 1030.
(75) Zussman, A. *J. Chem. Phys.* **1973**, *58*, 1514.
(76) Kruk, D.; Altmann, J.; Fujara, F.; Gädke, A.; Nolte, M.; Privalov, A. F. *J. Phys.: Condens. Matter* **2005**, *17*, 519.

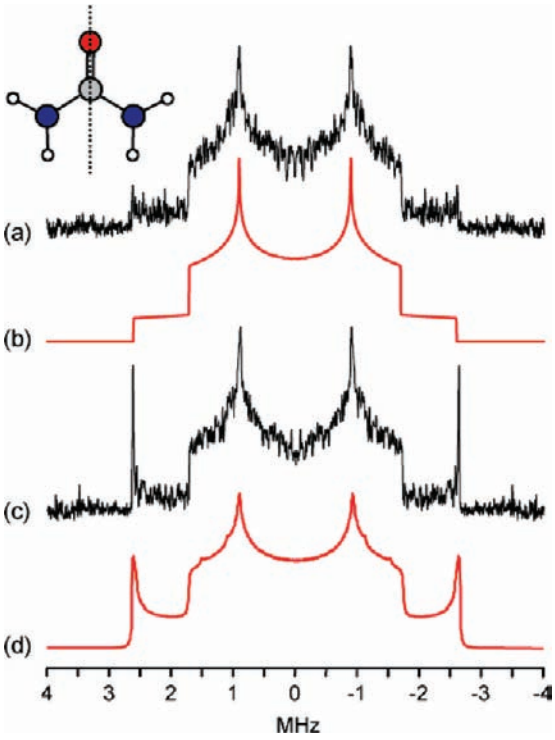

Figure 6. (a) ^{14}N WURST-echo spectrum of urea-d_4, with a fitted simulation (b) made using $C_Q = 3.47$ MHz and $\eta_Q = 0.31$. (c) The WURST-QCPMG spectrum, with a simulation (d) taking into account the flipping of the molecule around the C═O bond (see section 3.5 for further details). An image of the urea molecule is shown inset (nitrogen atoms in blue, carbon in gray and oxygen in red), with the flip axis indicated as a dotted line.

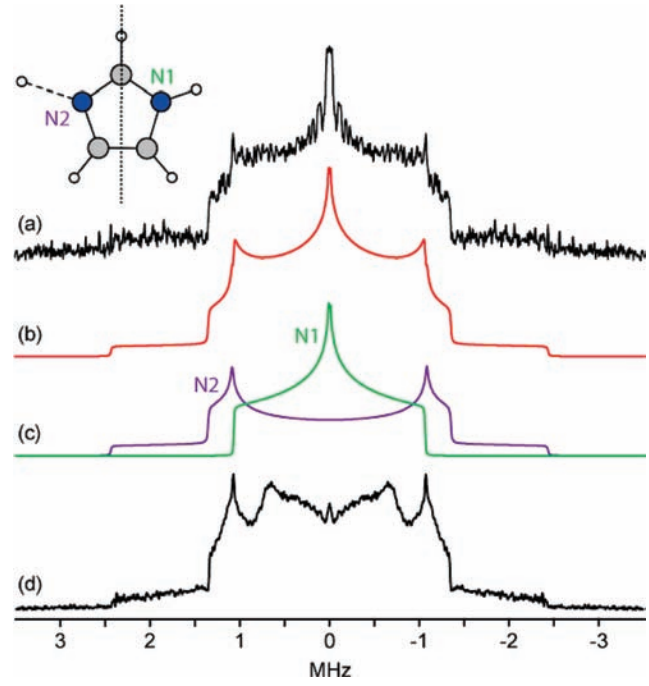

Figure 7. (a) ^{14}N WURST-echo spectrum of imidazole, (b) total fitted simulation, and (c) individual simulated line shapes with parameters $C_Q = 1.43$ MHz and $\eta_Q = 0.98$ (N1, green) and $C_Q = 3.25$ MHz and $\eta_Q = 0.15$ (N2, purple). (d) The WURST-QCPMG spectrum. An imidazole molecule is shown inset with the two nitrogen sites labeled (nitrogen atoms in blue, carbon in gray). The dashed line represents a hydrogen bond. The dotted line indicates the flip axis for the molecular reorientation mechanism (see section 3.6 for discussion).

to the effects of molecular dynamics that are not accounted for in the calculations. Unlike the rotation of the NH_3 groups in the hydrazine sample, however, the flipping of the urea molecule alters the orientation of the ^{14}N EFG tensor with respect to B_0, thereby affecting the ^{14}N NMR line shape. Figure 6c shows the WURST-QCPMG spectrum, which features sharp protrusions at the outermost edges. These regions correspond to crystallite orientations where the flipping mechanism does not alter the orientation of the EFG tensor with respect to B_0; thus, these crystallites have longer T_2 values and show greater QCPMG enhancement. Figure 6d was generated using the EXPRESS software, with an echo delay of 40 μs and a jump rate of 2×10^4 s^{-1}. The molecular flipping was modeled as a reorientation of the EFG tensor between Euler angles of $\alpha = 30°$, $\beta = 90°$, $\gamma = 0°$ and $\alpha = 210°$, $\beta = 270°$, $\gamma = 0°$. This simulation reproduces the sharp features at the edges of the pattern. The WURST-QCPMG spectrum, however, corresponds to a wide range of effective echo delays since it represents a sum of several echoes formed at different points in time. In order to extract accurate jump rates from the experimental data, individual echoes were processed and fitted to similar simulations. The resultant jump rate at 19 °C was determined as 7×10^3 s^{-1}, and further measurements made at other temperatures allowed an estimate of the activation energy for this process as $E_A = 75 \pm 15$ kJ mol^{-1}.[28]

3.6. Imidazole. The imidazole molecule forms the side chain of the amino acid histidine and thus constitutes an important component in many protein structures, with the heterocycle providing bonding sites for metal ions such as zinc or cobalt. As such, it is a system for which the nitrogen NMR interaction tensors have previously been well characterized (*vide infra*). The imidazole crystal structure features two chemically distinct nitrogen environments that are each involved in the same N—H···N hydrogen bond. For site N1, the proton is at a distance of 1.038 Å (i.e., it is bonded to the nitrogen) and is in the molecular plane. For site N2, the proton is at a distance of 1.828 Å, and the N—H vector forms an angle of ca. 14° with the plane of the molecule. These distances are taken directly from the neutron diffraction structure,[47] in which proton positions have been accurately determined. Optimization of these proton positions in CASTEP therefore did not result in as dramatic an improvement in the calculated NMR parameters as in other systems whose structures were determined by X-ray techniques (e.g., the other samples in Table 2 and a previous study of L-leucine),[27] and proton positions were only slightly altered.

The WURST-echo spectrum obtained from imidazole is shown in Figure 7a, and a fitted line shape made using two powder patterns of equal integrated intensity (Figure 7b,c) resulted in experimental parameters that agree very well with values predicted by plane-wave DFT (Table 2), as well as values measured using ^{14}N NQR[77] ($C_Q = 1.424$, $\eta_Q = 0.980$ for N1 and $C_Q = 3.267$, $\eta_Q = 0.129$ for N2). Garcia et al.[78] used NQR to determine the EFG tensor orientations in the molecular frame. For site N1, they concluded that the value of C_Q is negative and that the V_{11} component is aligned in the direction of the N—H bond, while V_{33} is perpendicular to the molecular plane. The CASTEP results obtained from the unaltered neutron

(77) Hunt, M. J.; Mackay, A. L.; Edmonds, D. T. *Chem. Phys. Lett.* **1975**, *34*, 473.
(78) Garcia, M. L. S.; Smith, J. A. S.; Bavin, P. M. G.; Ganellin, C. R. *J. Chem. Soc., Perkin Trans.* **1983**, *2*, 1391.

diffraction structure are in agreement with this, but after an optimization of the protons, the sign of C_Q becomes positive and the directions of the V_{33} and V_{22} components are swapped. This does not imply that the proton optimization process makes significant changes to the structure but rather is a result of the asymmetry parameter being close to 1, which means that $|V_{33}| \approx |V_{22}|$. Hence, only a relatively small change in the magnitude of the EFG in either of these directions can "swap" these components. A similar effect was observed in a ^{14}N NMR study of proline,[27] which also has an η_Q value close to unity. We note that a separate study of imidazole, which considered the effects of ^{14}N residual dipolar couplings on a ^{13}C CPMAS spectrum, also concluded that the C_Q for site N1 should be negative.[79] For site N2, the calculated C_Q is negative both before and after proton optimization, and the orientation of the EFG (V_{33} pointing toward the lone pair orbital and V_{11} perpendicular to the ring plane) is in agreement with that determined by Garcia et al.[78]

Ueda et al. measured the nitrogen CS tensors for both sites in imidazole directly from the static powder pattern obtained from a ^{15}N-enriched sample,[80] and these values are quoted in Table 2. The parameters predicted by plane-wave DFT before and after proton optimization show approximately the same level of agreement with experiment. As for the orientations of the shielding tensors in the molecular frame, Solum et al.[81] performed DFT calculations on a wide range of five- and six-membered nitrogen heterocycles and concluded that, for imino groups (such as site N1 in imidazole), σ_{11} is always in the radial direction of the ring (i.e., pointing toward the proton), while for "non-substituted" nitrogens (i.e., N2), it is tangential to the ring. In addition, they predicted that σ_{33} is always perpendicular to the ring plane. The shielding tensor directions predicted by our CASTEP calculations are in full agreement with these conclusions.

The WURST-QCPMG spectrum, which is shown in Figure 7d, shows significant distortions, once again indicating the presence of T_2 anisotropy caused by dynamic effects. The imidazole crystal structure consists of infinite chains of molecules along the *c*-axis, linked together by hydrogen bonds between the two nitrogen sites.[47] An enhanced proton conductivity along this axis was reported several decades ago, and a two-stage Grotthus mechanism was proposed to explain this.[82] The first stage involves proton hopping (PH) across the hydrogen bonds, and the second involves a molecular reorientation (MR) of the imidazole rings such that the chain is returned to its original state. The MR, which involves the breaking of the strong hydrogen bond and a 180° flip about the axis shown in Figure 7, is expected to be the rate-determining step, with an early ^{1}H relaxation study proposing a reorientation rate of ca. 1 s^{-1}.[83] More recent molecular dynamics results suggest that PH can occur very easily and that inversion defects in which the hydrogen-bonding direction is reversed along an entire chain are relatively stable.[84] However, evidence against fast PH in the bulk crystalline phase has been provided by ENDOR[85] and NQR experiments[77,86] as well as neutron diffraction, which suggests localization of the proton on a single, well-defined site on one side of the hydrogen bond.[47] Efforts to observe slow PH by ^{15}N cross-polarized MAS NMR exchange experiments[80,87] were unsuccessful and also appeared to rule out MR.[87] Further ^{1}H and ^{15}N NMR experiments by Goward, Spiess, and co-workers, however, revealed the presence of two distinct domains: a crystalline phase in which dynamics are absent and both ^{1}H and ^{15}N relaxation times are very long, and a disordered region in which exchange occurs between the two nitrogen sites and relaxation is much faster.[88,89] These latter findings indicate that the proton conduction mechanism in imidazole occurs primarily in disordered regions such as grain boundaries, and the question of anisotropic conductivity in the bulk crystal phase appears to remain unresolved.

The PH and MR mechanisms would each modulate the ^{14}N EFG tensors in distinct ways; thus, ^{14}N NMR could potentially shed light on these processes. The former mechanism would interchange the N1 and N2 EFG tensors (analogous to chemical exchange), while the latter would flip them individually by 180° (a process similar to the urea dynamics discussed above). These mechanisms should therefore be distinguishable via their very different effects on the ^{14}N NMR line shape, and EXPRESS simulations are shown in Figure 8a−c for respectively PH, MR, and both simultaneous processes. In the latter case, the simulations incorporate equal jump rates for both processes, though in reality the MR would be expected to be much slower. In fact, MR at a rate of 1 s^{-1} (as suggested from ^{1}H experiments)[83] would not have an observable effect on the ^{14}N spectrum. It is unsurprising, then, that the experimental spectra in Figure 8d more closely match the line shapes simulated with the PH mechanism only. These spectra were reconstructed from the first, fourth, and thirtieth echoes of each WURST-QCPMG train (corresponding to effective echo delay times of 177, 708, and 5310 μs, Figure 8d(i)−(iii), respectively). The line shapes match reasonably well with simulations of the PH mechanism at various jump rates. A concentrated effort at fitting these line shapes, however, indicates the presence of two separate domains, in agreement with the findings of Goward and Spiess.[88,89] This is most easily illustrated by considering the simulations in Figure 9, which show how the ^{14}N powder pattern changes over a range of both jump rates and echo delays under the PH model. Two regimes can be distinguished. For $k \leq 3 \times 10^5$ s^{-1} (referred to here as the slow motion regime), the line shapes at short echo delay times correspond to the static ^{14}N powder pattern resulting from the two separate nitrogen sites (as shown in Figure 7b). As the echo delay time is increased, the line shapes diverge from this. Conversely, for $k \geq 1 \times 10^6$ s^{-1} (the fast motion regime), line shapes at short echo delay times represent motionally averaged powder patterns arising from the interchange of the two EFG tensors. As the echo delay times are increased, line shapes in both of these regimes all eventually converge to an identical, "intermediate" line shape. This can

(79) Grasselli, M.; Díaz, L. E.; Olivieri, A. C. *Spectrosc. Lett.* **1991**, *24*, 895.
(80) Ueda, T.; Masui, H.; Nakamura, N. *Solid State Nucl. Magn. Reson.* **2001**, *20*, 145.
(81) Solum, M. S.; Altmann, K. L.; Strohmeier, M.; Berges, D. A.; Zhang, Y.; Facelli, J. C.; Pugmire, R. J.; Grant, D. M. *J. Am. Chem. Soc.* **1997**, *119*, 9804.
(82) Kawada, A.; McGhie, A. R.; Labes, M. M. *J. Phys. Chem.* **1970**, *52*, 3121.
(83) Daycock, J. T.; Jones, G. P.; Evans, J. R. N.; Thomas, J. M. *Nature* **1968**, *218*, 672.
(84) Iannuzzi, M. *J. Chem. Phys.* **2006**, *124*, 204710.
(85) Gloux, P.; Lamotte, B. *Mol. Phys.* **1972**, *24*, 23.
(86) Schempp, E.; Bray, P. J. *Phys. Lett. A* **1967**, *25*, 414.
(87) Hickman, B. S.; Mascal, M.; Titman, J. J.; Wood, I. G. *J. Am. Chem. Soc.* **1999**, *121*, 11486.
(88) Goward, G. R.; Schuster, M. F. H.; Sebastiani, D.; Schnell, I.; Spiess, H. W. *J. Phys. Chem. B* **2002**, *106*, 9322.
(89) Fischbach, I.; Spiess, H. W.; Saalwächter, K.; Goward, G. R. *J. Phys. Chem. B* **2004**, *108*, 18500.

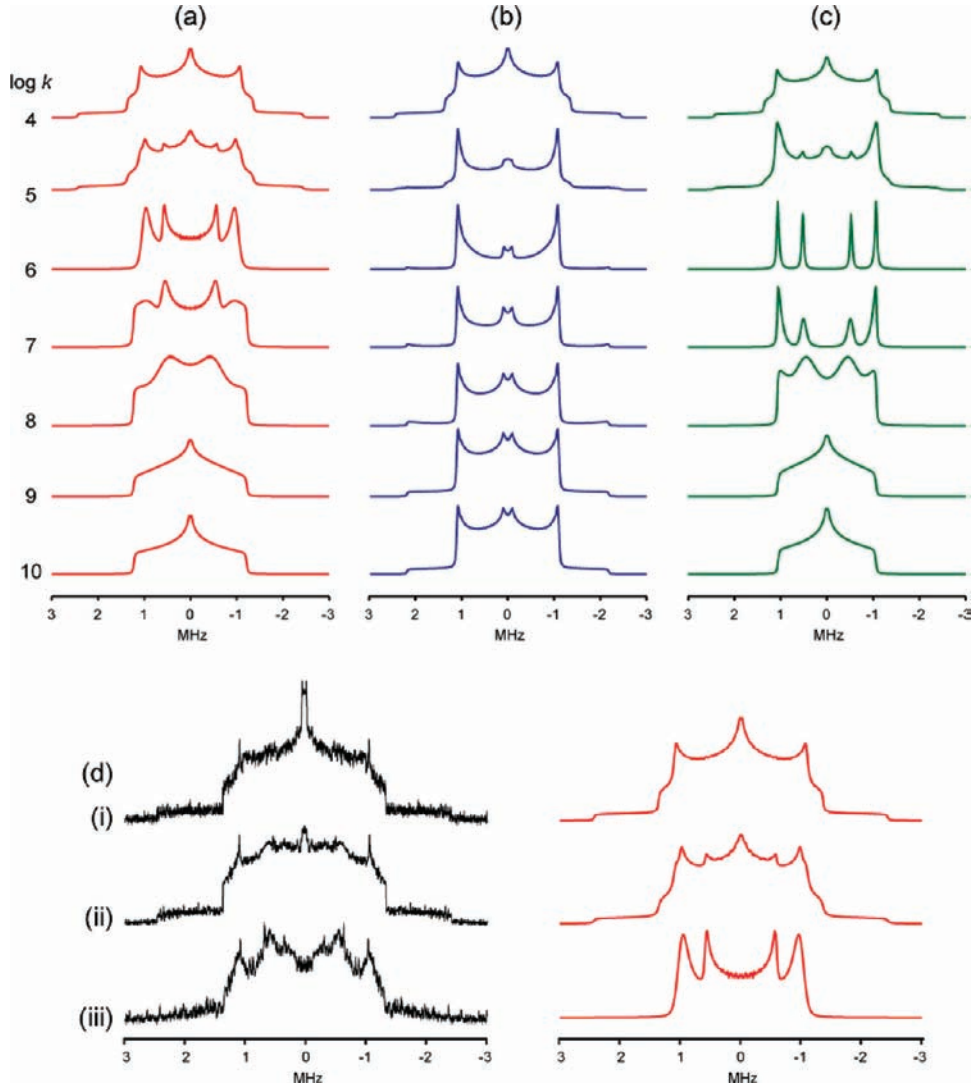

Figure 8. EXPRESS simulations of the ^{14}N powder pattern of imidazole undergoing (a) proton hopping across the hydrogen bond, (b) 180° molecular reorientation about an axis perpendicular to the N−N vector, and (c) both mechanisms. Jump rates used in the simulations are shown on the left (log *k*). (d) Experimental spectra reconstructed from the (i) first, (ii) fourth, and (iii) thirtieth echoes in the QCPMG trains of each piece, alongside simulations incorporating the effects of the proton hopping mechanism.

be seen to occur in Figure 9 for k values between 3×10^4 and 1×10^7 s^{-1}, which all show the same line shape at an echo delay of 256 μs. It follows that the observation of both slow/static and motionally averaged (fast regime) line shapes from the experimental WURST-QCPMG echo train (Figure 8d(i) and (iii), respectively) could only be caused by the presence of at least two k values, one in each regime. The slow/static domain clearly makes up the majority of the sample, based on the good agreement between the WURST-echo spectrum and the fitted simulation in Figure 7. By the 30th echo of the QCPMG train, however, the line shape is dominated by a fast regime-like line shape (Figure 8d(iii)). The presence of two domains, one with slow (or no) PH and one with fast PH, would also explain the appearance of the WURST-QCPMG spectrum in Figure 7d, which has characteristics of both the slow and fast regime line shapes. Our attempts to obtain a convincing fit of the experimental WURST-QCPMG spectrum were unsuccessful, being complicated by numerous variables such as the relative proportions of each domain, their individual T_2 values and T_2 anisotropies, and also the computational difficulties mentioned in section 2.3. Attempts to selectively observe these domains individually on the basis of possible differences in T_1 relaxation were also unsuccessful. From the spectra and simulations in Figures 8d and 9, however, the minimum PH jump rate in the fast PH domain can be estimated to be ca. 1×10^8 s^{-1} at room temperature. To summarize this analysis, the experimental ^{14}N NMR data obtained from imidazole are best interpreted as arising from both a bulk imidazole structure with relatively slow (or no) PH present and a less abundant domain in which PH occurs much more quickly. Such conclusions are fully consistent with the work of Goward and Spiess,[88,89] as well as all other experimental studies mentioned above, providing further support for the proposal that the proton conduction in this material occurs via disordered domains such as grain boundaries rather than the bulk crystal lattice.

In the preceding three sections, we have shown that ^{14}N NMR line shapes from samples with very large C_Q values can be used to access information on molecular dynamics in two distinct ways. In the case of hydrazine dihydrochloride, the EFG tensor remains static while local dynamics give rise to an orientational dependence in N−H dipolar couplings, causing an anisotropy in transverse dephasing, observable as a variation in QCPMG enhancement across the powder pattern. For samples in which the dynamics modulate the EFG tensor on a time scale

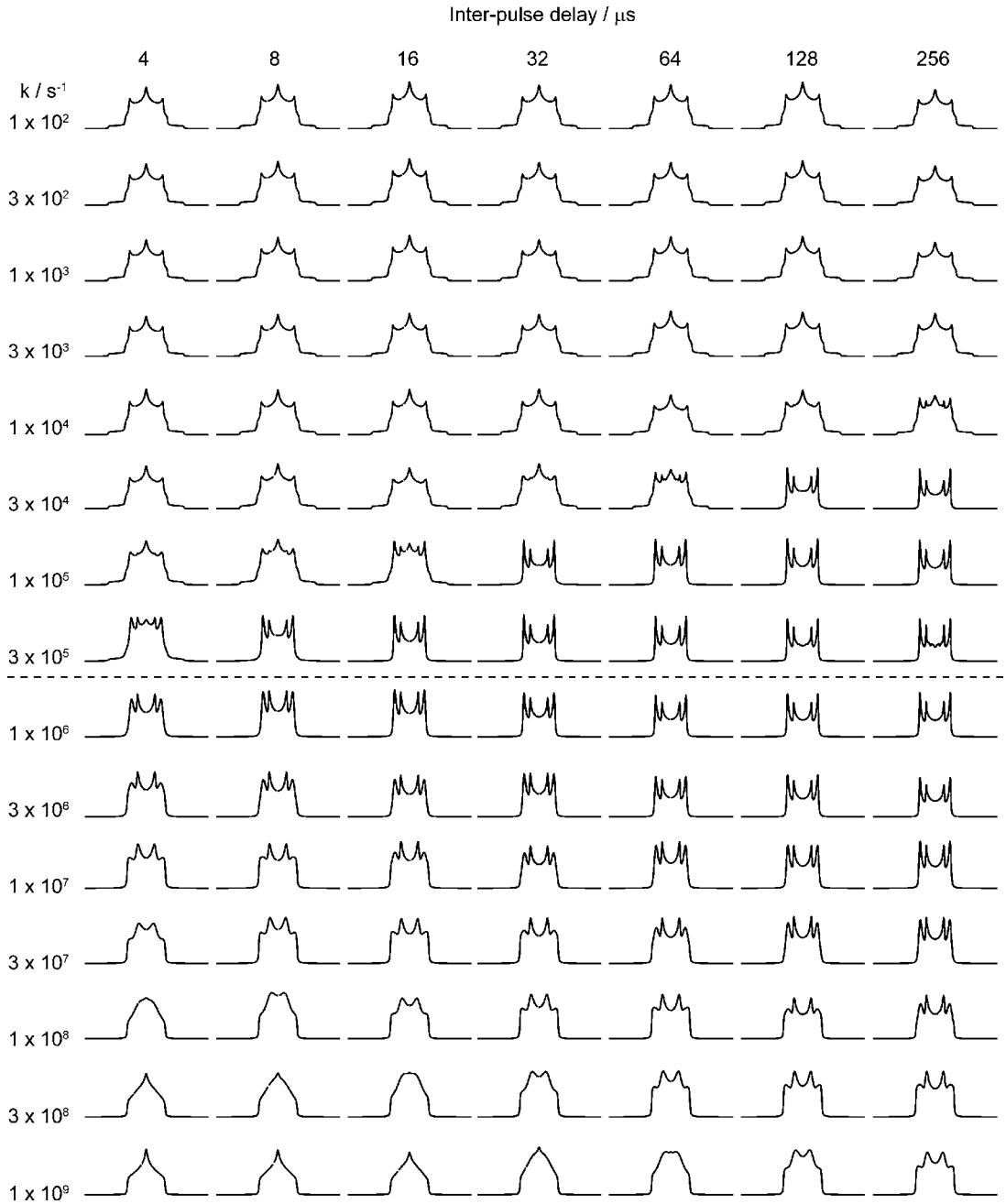

Figure 9. EXPRESS simulations of the ^{14}N powder pattern of imidazole undergoing proton hopping across the hydrogen bond, with various jump rates and echo delays as shown. The dashed line separates the slow and fast motion regimes. The simulations are shown with normalized heights.

comparable to C_Q^{-1}, jump rates can be quantified in a way that is a direct analogy to more commonly used ^{2}H echo or QCPMG NMR experiments.[90,91] Prior to our recent communication,[28] ^{14}N NMR had only been used in this way once before, on choline salts with extremely small ^{14}N C_Q values (>70 kHz), for which the entire ^{14}N NMR spectrum could be recorded using conventional methods.[92] Ultra-wideline ^{14}N NMR can therefore provide an attractive complement to previously reported ^{14}N methods for studying molecular dynamics, such as hole-burning[93] or indirectly detected HMQC-type experiments.[4,94]

3.7. Melamine. Melamine, whose molecular structure is shown inset in Figure 10, is the trimer of cyanamide and was the first crystal structure to be determined from X-ray experiments by least-squares refinement.[95] In the crystal structure, which was subsequently further refined,[48] the molecule shows large deviations from planarity, with N−C−N−H dihedral angles as large as 24°. Although all six nitrogen atoms in the molecule sit at unique crystallographic sites, resolving these sites

(90) Batchelder, L. S. In *Encyclopedia of Nuclear Magnetic Resonance*; Grant, D. M., Harris, R. K., Eds.; Wiley: Chichester, 1996; Vol. 3, p 1574.
(91) Larsen, F. H.; Jakobsen, H. J.; Ellis, P. D.; Nielsen, N. C. *Chem. Phys. Lett.* **1998**, *292*, 467.
(92) Pratum, T. K.; Klein, M. P. *J. Magn. Reson.* **1989**, *81*, 350.
(93) Hill, E. A.; Yesinowski, J. P. *J. Chem. Phys.* **1997**, *107*, 346.
(94) Cavadini, S.; Abraham, A.; Ulzega, S.; Bodenhausen, G. *J. Am. Chem. Soc.* **2008**, *130*, 10850.
(95) Hughes, E. W. *J. Am. Chem. Soc.* **1941**, *63*, 1737.

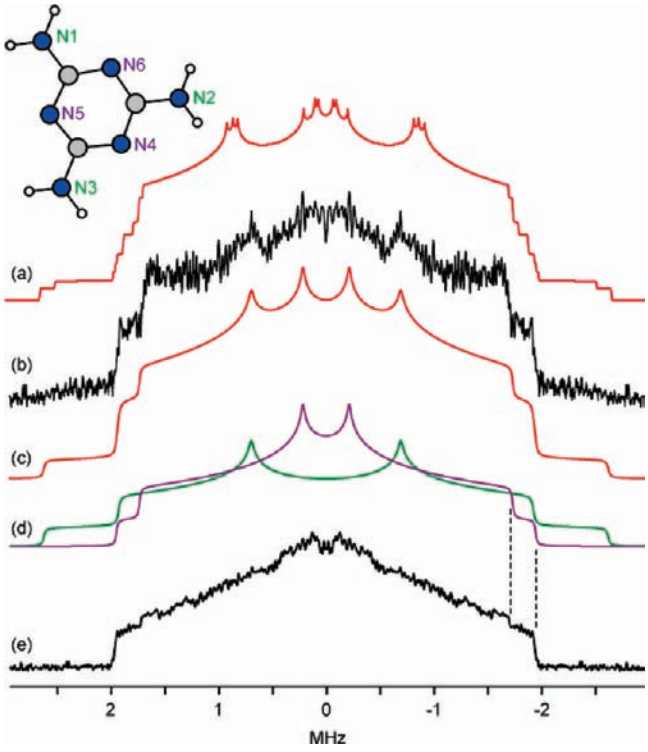

Figure 10. (a) Simulation of the ^{14}N NMR spectrum of melamine using parameters for all six sites predicted by CASTEP. (b) ^{14}N WURST-echo spectrum of melamine. (c) A fit comprised of two powder patterns (in (d)) of equal integrated intensity. (d) The two individual fitted patterns with parameters $C_Q = 3.50$ MHz, $\eta_Q = 0.47$ (N1, N2, and N3, green) and $C_Q = 2.60$ MHz, $\eta_Q = 0.78$ (N4, N5, and N6, purple). (e) The ^{14}N WURST-QCPMG spectrum. The melamine molecule is shown inset with labeled sites (nitrogen atoms in blue, carbon in gray).

in the ^{14}N NMR spectrum would require both an extremely high resolution and large S/N ratio (see the simulated spectrum in Figure 10a, which was made with the parameters for all six sites predicted by CASTEP). We therefore fitted the WURST-echo spectrum to two powder patterns of equal intensity, one for the amine nitrogens and another for the ring nitrogens (Figure 10b−d). The resultant experimental parameters, $C_Q = 3.50$ MHz, $\eta_Q = 0.47$ (amine nitrogens) and $C_Q = 2.60$ MHz, $\eta_Q = 0.78$ (ring nitrogens), are in reasonable agreement with the average values predicted by CASTEP for each set of sites (see Table 2).

The calculated EFG and CS tensor orientations for the amine nitrogens are very similar to those in urea (see section 3.5), with V_{33} and σ_{22} approximately perpendicular to the ring plane and V_{22} and σ_{33} roughly parallel to the N−C bonds, although the melamine molecule's departure from planarity results in deviations from urea's "ideal" amine tensor orientations that differ for each site (as well as values of the Euler angle β that deviate from 90°). The calculated CS tensor orientations for the ring nitrogens in melamine are such that σ_{33} is perpendicular and σ_{11} is tangential to the ring, which is consistent with the N2 site in imidazole and the conclusions of Solum et al.[81] The EFG tensor orientations predicted by plane-wave DFT for these sites, however, are different, with V_{11} perpendicular to the ring plane but V_{33} tangential to the ring, rather than radial as for the imidazole N2 site. There is also a large difference in both C_Q and η_Q for the ring nitrogens in melamine and imidazole. This difference is likely due to the fact that the imidazole N2 site is involved as a proton-acceptor in a hydrogen bond, whereas the ring nitrogens in melamine are not, with the nearest protons

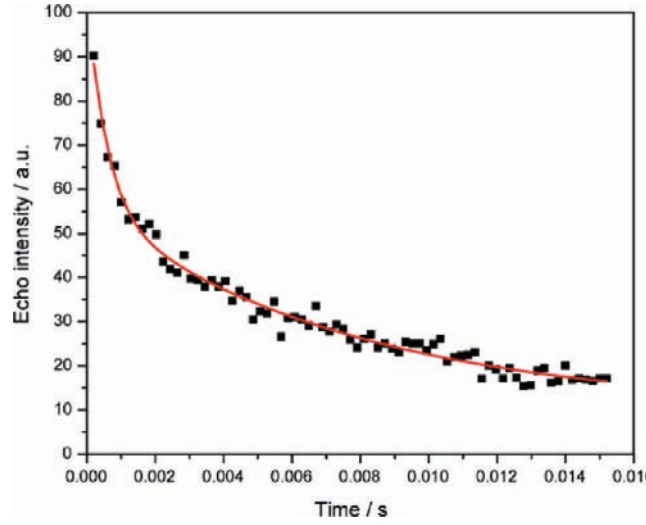

Figure 11. Decay of the echo intensity measured from the QCPMG train acquired from melamine at an offset of −1.0 MHz. The red line is a biexponential fit.

being over 2 Å distant. The difference in asymmetry parameters predicted by plane-wave DFT between sites N5 ($\eta_Q = 0.79$) and N4 and N6 ($\eta_Q = 0.93$ and 0.90, respectively) is due to the N5 site being coordinated to two protons from two different neighboring molecules, forming a pseudotetrahedral environment, while N4 and N6 are coordinated to just one, forming an environment that is closer to a planar, three-coordinate configuration.

^{15}N isotropic chemical shifts for the six nitrogen sites in melamine have been previously determined by Damodaran et al. using a ^{15}N-enriched sample.[96] Two of the ring nitrogens show very similar chemical shifts, which leads to a single ^{15}N MAS peak of double intensity. Understandably, the authors assigned this shift to the ring nitrogens with the most similar chemical environments (i.e., those coordinated to single protons, N4 and N6). Our CASTEP calculations on both the unaltered and proton-optimized structures, however, suggest that it is actually sites N5 and N6 that have the closest chemical shifts, and we have therefore assigned the experimental isotropic shifts for these ring nitrogens accordingly (see Table 2).

Finally, we note that the WURST-QCPMG spectrum (Figure 10e) is markedly different in shape from the WURST-echo spectrum. In fact, it closely resembles the fitted powder pattern for the three ring nitrogen sites, with the two outermost pairs of shoulders clearly visible and in line with the simulation. Attempts to reproduce this line shape by modeling various dynamic mechanisms in EXPRESS, such as amide group rotation or full molecular C_3 rotation, were unsuccessful (and in any case, such dynamics would be expected to have prohibitively large energy barriers; for example, the rotational barrier for the amine group has been predicted to be over 60 kJ mol^{-1} in the *gas* phase).[97,98] We therefore attribute this effect to a difference in transverse relaxation rates between the ring and amine nitrogens, the relaxation being slower for the former sites, thus causing them to be preferentially selected by the QCPMG protocol. To confirm this, we attempted to fit the decay

(96) Damodaran, K.; Sanjayan, G. J.; Rajamohanan, P. R.; Ganapathy, S.; Ganesh, K. N. *Org. Lett.* **2001**, *3*, 1921.
(97) Meier, R. J.; Coussens, B. *J. Mol. Struct. Theochem.* **1990**, *209*, 303.
(98) Meier, R. J.; Maple, J. R.; Hwang, M.-J.; Hagler, A. T. *J. Phys. Chem.* **1995**, *99*, 5445.

Table 3. Calculated Nitrogen EFG Tensor Components for 1,4-Dicyanobenzene: Monomer and Tetramer Structures

	V_{33} (au)	V_{22} (au)	V_{11} (au)	C_Q (MHz)	η_Q
Monomer	-0.893	0.467	0.426	-4.29	0.05
Tetramer	-0.778	0.430	0.348	-3.74	0.11
Δ(Monomer-Cluster)	-0.115	0.037	0.078	-0.55	-0.06

NLMO Contributions to V_{33} (in au)[1]

	Monomer		Tetramer		Δ(Monomer-Cluster)
	Lewis	non-Lewis	Lewis	non-Lewis	
σ(N-C)	-1.985	-0.003	-1.948	-0.006	-0.034
$\pi(N\text{-}C)_A$	1.126	0.002	1.131	0.001	-0.004
$\pi(N\text{-}C)_B$	1.108	0.003	1.122	0.000	-0.011
LP(N)	-1.697	0.005	-1.760	0.009	0.059
Core(C)	-0.330	-0.002	-0.361	-0.002	0.031
σ(C-C)			-0.115	0.003	0.112
Sum	**-1.778**	**0.005**	**-1.931**	**0.005**	**0.153**
Σ(small terms)[2]	0.880		1.148		-0.268

[1] Shaded regions contain values which are referred to directly in the text. [2] All terms greater than 0.100 au are included in the table. More distant molecular orbitals make small contributions to the EFG at the relevant nitrogen, and the sum of all these small terms (both Lewis and non-Lewis) is included here for completeness.

of the QCPMG echo intensities from the experimental piece acquired at −1.0 MHz. This fit is shown in Figure 11, and the biexponential nature of the decay is clearly visible (Figure S2 in the Supporting Information shows a comparison with a single-exponential fit). The T_2 relaxation times obtained from this fit are 0.6 ± 0.1 and 8 ± 1 ms, and we assign these to the amine and ring nitrogen sites, respectively. The more rapid transverse relaxation rate for the amine nitrogens would perhaps be expected, arising from modulations of N−H dipolar couplings caused by vibrational modes present in these groups. This illustrates the potential of the QCPMG protocol in selectively observing nitrogen sites on the basis of differences in transverse relaxation times, a strategy which can potentially be used to simplify crowded spectra and to improve simulations of the echo line shape, resulting in more accurate and quantitative fits.

4. NLMO Analysis of ^{14}N EFG Tensors

Given the ubiquity of the structural motifs discussed herein, we have undertaken DFT calculations aimed at analyzing the contributions of key molecular orbitals to the ^{14}N EFG tensors. EFG tensors were analyzed in terms of natural localized molecular orbitals (NLMOs) utilizing the ADF software package. A full description of the theoretical basis of this work can be found elsewhere.[99] These analyses allow for the evaluation of the relationships between the local electronic structure and the ^{14}N EFG tensors, as well as the influence of intermolecular interactions on these relationships. The systems we chose to examine are 1,4-dicyanobenzene, urea, and imidazole. Results from all of the calculations described below are summarized in Tables 3, 4, and 5, respectively.

Since calculations on both monomers and clusters were conducted, it was of primary importance to determine the cluster sizes for which agreement is achieved between experimental results, calculations on finite clusters, and calculations on infinite-periodic systems. Plots of theoretical values of C_Q and η_Q as a function of cluster size and their comparison to values obtained from experiment and CASTEP calculations are presented and discussed in section S3 of the Supporting Information. The EFG tensor parameters calculated with the cluster models converge to the plane-wave DFT values for cluster sizes

(99) Autschbach, J.; Zheng, S.; Schurko, R. W. *Conc. Magn. Reson. A* **2010**, *36*, 84.

Table 4. Calculated Nitrogen EFG Tensor Components for Urea: Monomer and 11-Mer Structures

	V_{33} (au)	V_{22} (au)	V_{11} (au)	C_Q (MHz)	η_Q
Monomer	-1.020	0.541	0.480	-4.90	0.06
11-mer	-0.790	0.523	0.267	-3.80	0.32
Δ(Monomer-Cluster)	-0.230	0.018	0.212	-1.10	-0.26

NLMO Contributions to V_{33} (in au)[1]

	Monomer		11-mer		Δ(Monomer-Cluster)
	Lewis	non-Lewis	Lewis	non-Lewis	
σ(N-C)	0.913	-0.001	0.960	0.005	-0.053
$\sigma(N\text{-}H)_A$	1.044	-0.006	1.104	-0.001	-0.065
$\sigma(N\text{-}H)_B$	1.049	-0.008	1.113	-0.001	-0.071
π(N-C)	-3.838	0.074	-3.677	0.131	-0.218
Core(C)			0.115	0.001	-0.116
Sum	**-0.832**	**0.059**	**-0.385**	**0.135**	**-0.523**
Σ(small terms)[2]	-0.247		-0.540		0.293

NLMO Contributions to V_{11} (in au)

	Monomer		11-mer		Δ(Monomer-Cluster)
	Lewis	non-Lewis	Lewis	non-Lewis	
σ(N-C)	-1.428	0.002	-1.890	-0.006	0.470
$\sigma(N\text{-}H)_A$	1.080	-0.012	-0.158	-0.001	1.227
$\sigma(N\text{-}H)_B$	-1.035	0.002	0.601	-0.006	-1.628
π(N-C)	1.935	-0.045	1.835	-0.085	0.140
Sum	**0.552**	**-0.053**	**0.388**	**-0.098**	**0.209**
Σ(small terms)[2]	-0.019		-0.023		0.003

[1] Shaded regions contain values which are referred to directly in the text. [2] All terms greater than 0.100 au are included in the table. More distant molecular orbitals make small contributions to the EFG at the relevant nitrogen, and the sum of all these small terms (both Lewis and non-Lewis) is included here for completeness.

of four (1,4-dicyanobenzene), eleven (urea), and sixteen (imidazole), or larger.

4.1. 1,4-Dicyanobenzene. DFT calculations on 1,4-dicyanobenzene predict that V_{33} is oriented along the C≡N bond axis for both the monomer and tetramer (Figure 12a,b). The sign of V_{33} is negative in both cases, and the absolute magnitude of V_{33} is slightly larger in the monomer. As shown in Table 3, there are large negative contributions to V_{33} arising from the σ(N−C) and lone pair nitrogen [LP(N)] MOs in both systems, and smaller positive contributions from the two π(N−C) MOs; see Figure 12c for a depiction of the relevant MOs. The EFG tensor is slightly less axially symmetric in the tetramer, due to intermolecular electrostatic effects absent in the case of the monomer (see Supporting Information). Finally, in comparing the monomer and tetramer, large variations in the individual dominant contributions which account for the slight differences in C_Q and η_Q are not observed; rather, these differences result from the collective influence of an ensemble of smaller contributions. Hence, the ^{14}N EFG tensor in 1,4-dicyanobenzene is largely determined by the local structure, and a complex array of smaller contributions from intermolecular interactions contribute to differences in the asymmetry parameters for the monomer and cluster structures.

4.2. Urea. The influence of intermolecular interactions on the ^{14}N EFG tensor characteristics and orientations is more apparent in urea, which has strong hydrogen bonds between neighboring molecular units. This is especially evidenced by the significant differences in the EFG tensors calculated for the isolated molecule and 11-mer (Figure 13a,b). In both systems, V_{33} is predicted to lie perpendicular to the trigonal planar arrangement of atoms about the nitrogen center. V_{22} is oriented close to the N−C bond in both systems ($\angle(V_{22}\text{−N−C}) = 23.1°$ and 7.9° in the monomer and 11-mer, respectively). As in the case of the sp nitrogen in 1,4-dicyanobenzene, the signs of V_{33} are calculated to be negative, despite the distinct orientations of V_{33} in these two systems (i.e., V_{33} is not along a bond in urea). However, in

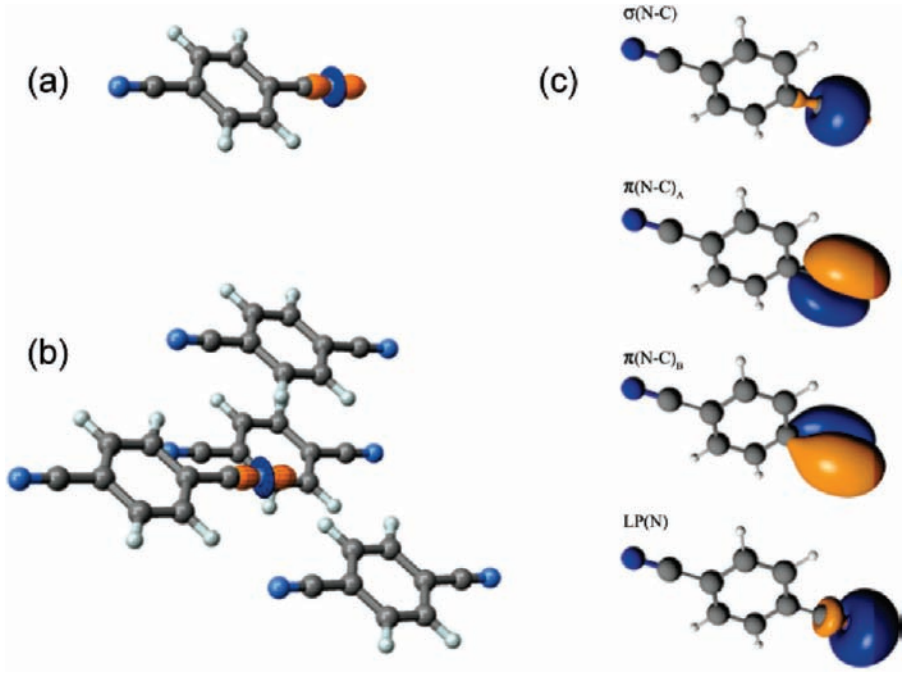

Figure 12. Results from DFT calculations of monomers and finite clusters of 1,4-dicyanobenzene using localized basis sets and the ADF software package. Calculated EFG tensors for (a) the monomer and (b) the tetramer of 1,4-dicyanobenzene. The EFG tensor is plotted as a surface showing the sign and symmetry visually, with orange representing negative and blue representing positive principal values; see ref 99 for further details. (c) Selected NLMOs from the monomers that are important to the analysis in section 4.1, labeled using the notation of Table 3.

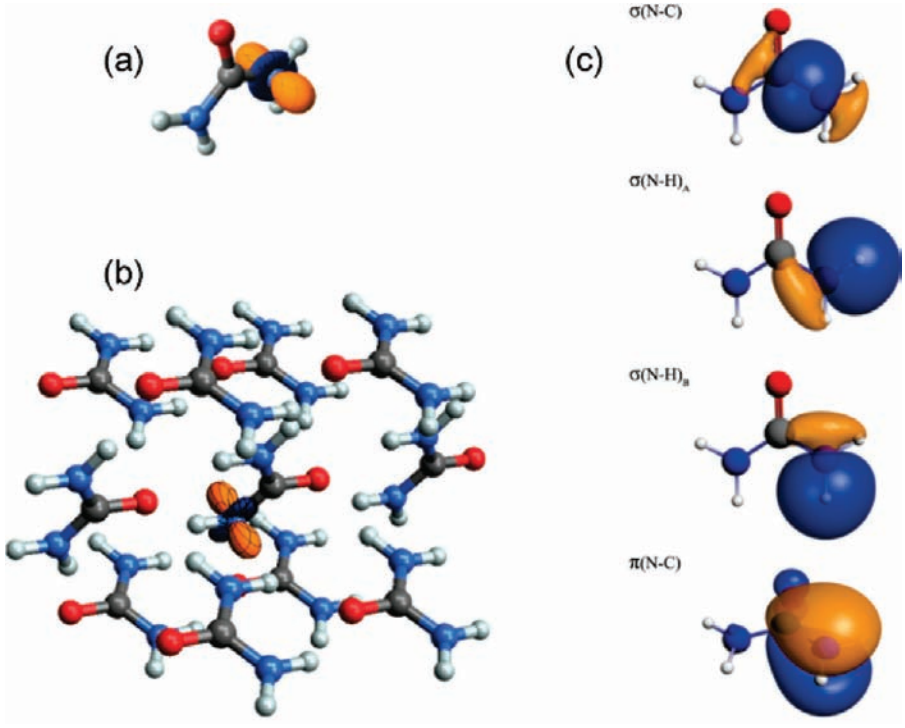

Figure 13. Results from DFT calculations of monomers and finite clusters of urea. Calculated EFG tensors for (a) the monomer and (b) the 11-mer of urea. (c) Selected NLMOs from the monomers that are discussed in section 4.2. See Table 4 for NLMO notation.

urea, the large negative contributions to V_{33} (Table 4) arise from the π(N−C) MO, which are only partially offset by smaller positive field gradients from the σ(N−C) and two σ(N−H) MOs (these MOs are depicted in Figure 13c).

The absolute magnitudes of V_{33} and V_{11} of the monomer are considerably larger than those of the 11-mer; these differences are significantly larger than those of 1,4-dicyanobenzene. Examination of the structure of the 11-mer, and the MOs in both the monomer and 11-mer, reveals that intermolecular N−H hydrogen bonding results in a reduction of the negative contribution from the π(N−C) MO and an increase in the positive contributions from the σ(N−C) and two σ(N−H) MOs, accounting for the reduced V_{33} in the 11-mer. The absolute magnitude of V_{11} is also reduced in the 11-mer, predominantly

Table 5. Calculated Nitrogen EFG Tensor Components for Imidazole Site N1 in Monomer and 16-Mer Structures

	V_{33} (au)	V_{22} (au)	V_{11} (au)	QCC (MHz)[1]	η_Q
Monomer	-0.558	0.367	0.191	-2.68	0.31
16-mer	0.314	-0.283	-0.031	-1.36	0.80
	V_{11}^M-V_{33}^C	V_{33}^M-V_{22}^C	V_{22}^M-V_{11}^C		
Δ(Monomer-Cluster)[2]	-0.123	-0.275	0.397		

NLMO Contributions to V_{33}(monomer) vs. V_{22}(cluster) (in au)[3]

	Monomer (V_{33})		16-mer (V_{22})		Δ(Monomer-Cluster)
	Lewis	non-Lewis	Lewis	non-Lewis	
σ(N-H)	1.069	-0.017	1.143	-0.009	-0.082
$\sigma(N\text{-}C)_A$	0.989	-0.001	1.050	0.006	-0.068
$\sigma(N\text{-}C)_B$	0.985	0.000	1.043	0.006	-0.064
$\pi(N\text{-}C)_A$	-3.587	0.206	-2.781	0.050	-0.650
$\pi(N\text{-}C)_B$			0.012	-0.396	0.384
Core(C)			0.116	0.001	-0.117
Core(C)			0.110	0.001	-0.111
Sum	**-0.544**	**0.188**	**0.693**	**-0.341**	**-0.708**
Σ(small terms)[4]	-0.202		-0.635		0.433

NLMO Contributions to V_{11}(monomer) vs. V_{33}(cluster) (in au)

	Monomer (V_{11})		16-mer (V_{33})		Δ(Monomer-Cluster)
	Lewis	non-Lewis	Lewis	non-Lewis	
σ(N-H)	1.145	-0.019	1.153	-0.013	0.014
$\sigma(N\text{-}C)_A$	-1.476	-0.006	-1.381	-0.010	0.091
$\sigma(N\text{-}C)_B$	-1.176	-0.011	-1.196	-0.007	-0.016
$\pi(N\text{-}C)_A$	1.798	-0.112	1.388	-0.026	-0.324
$\pi(N\text{-}C)_B$			0.012	0.193	0.205
Core(C)	-0.105	-0.001	-0.118	-0.001	-0.013
Sum	**0.186**	**-0.149**	**-0.142**	**0.136**	**0.043**
Σ(small terms)[4]	0.154		0.320		-0.166

NLMO Contributions to V_{22}(monomer) vs. V_{11}(cluster) (in au)

	Monomer (V_{22})		16-mer (V_{11})		Δ(Monomer-Cluster)
	Lewis	non-Lewis	Lewis	non-Lewis	
σ(N-H)	-2.214	0.036	-2.296	0.022	0.096
$\sigma(N\text{-}C)_A$	0.191	0.011	0.146	0.001	0.055
$\sigma(N\text{-}C)_B$	0.487	0.007	0.337	0.004	0.153
$\pi(N\text{-}C)_A$	1.788	-0.094	1.393	-0.024	0.325
$\pi(N\text{-}C)_B$			-0.024	0.203	-0.179
Sum	**0.252**	**-0.040**	**-0.444**	**0.206**	**0.450**
Σ(small terms)[4]	0.155		0.207		-0.053

[1] Because site N1 of imidazole is experimentally characterized by an η_Q value near 1, it is more sensible to compare the EFG along a certain direction than to compare C_Q directly (see discussion of CASTEP calculations for more information). Results for this site are therefore plotted using a quadrupolar coupling constant (QCC), analogous to C_Q, except using the EFG component perpendicular to the plane instead of V_{33} exclusively. [2] Differences between V_{ii} components with common alignments are presented here. Values in table cells with the same shading are compared above. See text for details. [3] Shaded regions of the NLMO lists contain values which are referred to directly in the text. [4] All terms greater than 0.100 au are included in the table. More distant molecular orbitals make small contributions to the EFG at the relevant nitrogen, and the sum of all these small terms (both Lewis and non-Lewis) is included here for completeness.

due to a very large change in the contribution from the $\sigma(N-H)_A$ MO (i.e., it is large and positive in the monomer but small and negative in the 11-mer). This undoubtedly arises from the influence of hydrogen bonding with neighboring units (for short NH···O contacts, the crystallographically determined NO distances are 2.96 and 3.01 Å). Hence, although the nitrogen EFG tensor is a local property in urea in the sense that the signs of the principal components and the orientation of the tensor are determined by the bonding and lone pair arrangement directly around the nucleus of interest,[99] it is strongly influenced in the solid state by the strong hydrogen-bonding network that alters the contributions from the π and σ MOs relative to those of the monomer.

4.3. Imidazole. The two nitrogen sites in imidazole have very different ^{14}N EFG tensor characteristics and orientations due to their disparate local environments. For the NH site (site N1), the ^{14}N EFG tensors in the monomer and 16-mer have V_{33} values of opposite sign and different orientations (Figure 14a). In the monomer, V_{33} is aligned perpendicular to the trigonal plane, and V_{22} is aligned close to the N−H bond ($\angle(V_{22}-N-H) = 3.8°$), whereas in the 16-mer, V_{22} is directed approximately perpendicular to the trigonal plane, and V_{11} is aligned very close to the NH bond ($\angle(V_{11}-N-H) = 1.4°$). Due to these distinct orientations, we will consider the following monomer/16-mer pairs of components together: V_{33}/V_{22}, V_{11}/V_{33}, and V_{22}/V_{11}. Decompositions of the MO contributions to these EFG components are given in Tables 5 and 6 for sites N1 and N2, respectively, with the MOs relevant to the following discussion depicted in Figure 14c−f.

The V_{33} (monomer) and V_{22} (16-mer) components are both predicted to be negative, dominated by large negative contributions from the π(N−C) MOs, though the absolute magnitude of this contribution is diminished in the 16-mer. The V_{33} (16-mer) and V_{11} (monomer) components are oriented in the trigonal plane, approximately perpendicular to the N−H bond. Both components are calculated to be positive. The V_{33} (16-mer) receives a small positive contribution from the $\pi(N-C)_A$ MO and has σ(N−C) and σ(N−H) contributions that are similar in magnitude to those of V_{11} in the monomer. V_{11} (monomer) receives an even larger positive contribution from the π(N−C) MO and, accordingly, is slightly more positive than V_{33} of the 16-mer. Finally, the V_{22} (monomer) and V_{11} (16-mer) components, which are aligned near the N−H bond, have similar contributions from all of their MOs except for the π(N−C) MOs; the contribution is significantly more positive in the former case, resulting in a positive V_{22}. The EFG along the NH bond is reduced to almost zero in the 16-mer, a difference which becomes strikingly obvious when viewing the tensor plots shown in Figure 14a,b.

In each case above, there are large differences in the EFG tensor contributions of the π(N−C) MOs, which are oriented perpendicular to the trigonal plane in both the monomer and 16-mer (Figure 14c,d). The $\pi(N-C)_A$ MO describes π-bonding in both systems; however, in the 16-mer, the MO is polarized toward the end of the five-membered ring with the N1 site. This MO is undoubtedly influenced by the presence of "π-stacking" of molecules in the cluster, which serves to alter the nature of this MO and reduce its contributions to the absolute magnitudes of all three EFG tensor components. Since all of the other components stay more or less the same, it is predominantly alterations to this MO which result in the different EFG tensor orientations and characteristics, making ^{14}N NMR a very useful probe of intermolecular interactions. It is important to note that we must attribute these MO changes to the close-range orbital overlap component of the π-stacking interactions, since DFT with standard functionals (such as those used here) is not able to describe the dispersion component of π-stacking properly.

For the N2 lone pair site, V_{33} is aligned near the direction of the nitrogen lone pair MO in the monomer and 16-mer (Figure 14a,b). V_{33} is predicted to be negative in both systems and is dominated by negative contributions from the LP(N) MO and positive contributions from the $\sigma(N-C)_B$ MOs. Hydrogen bonding appears to increase both the negative contribution of the LP(N) MO to V_{33} and the positive contribution of the $\sigma(N-C)_B$ MO for the 16-mer. There are also numerous other smaller contributions from other MOs which result in a net

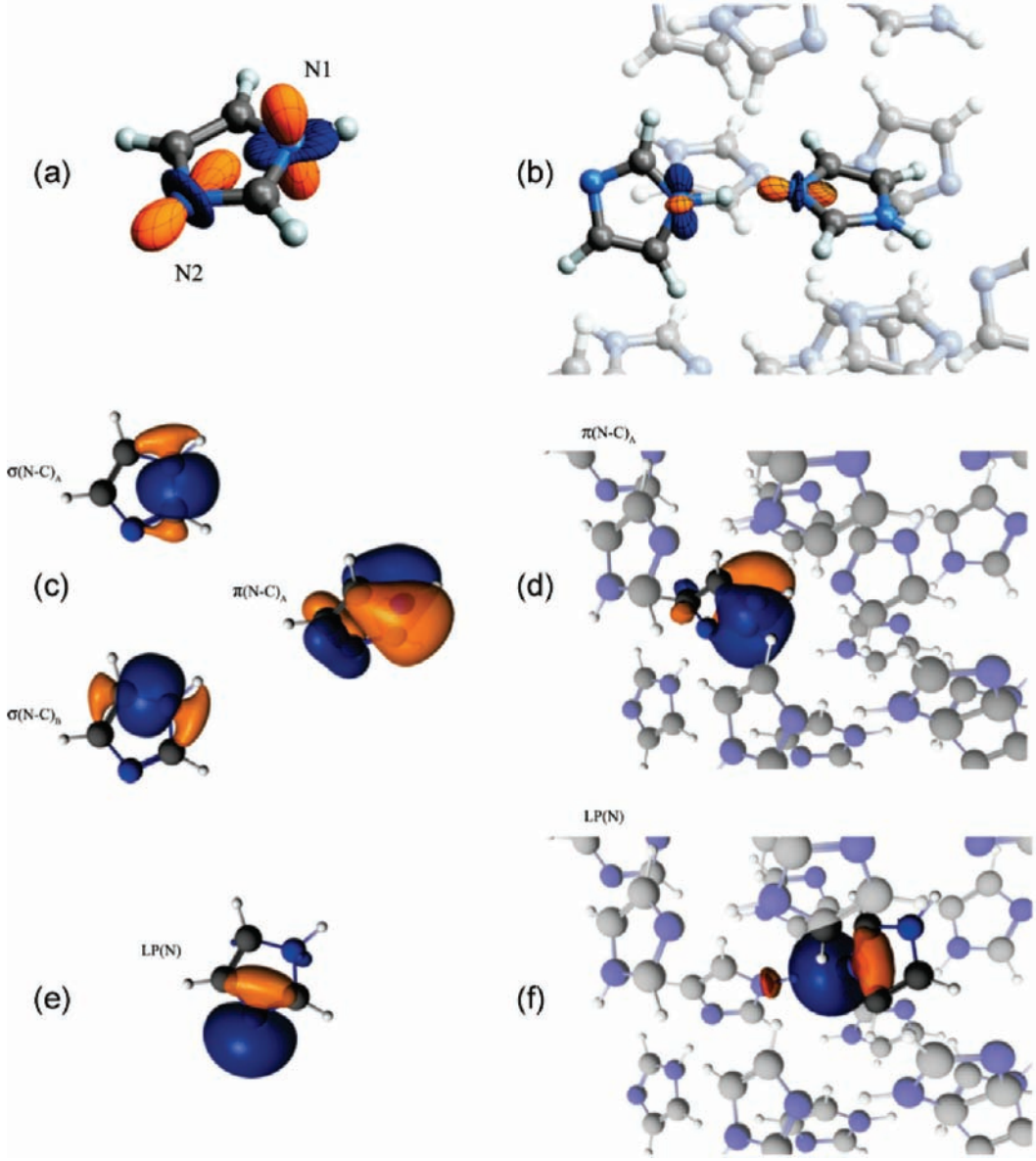

Figure 14. Results from DFT calculations of site N1 and site N2 in the monomer and 16-mer of imidazole and using localized basis sets and the ADF software package. Calculated EFG tensors for each site in (a) the monomer and (b) the 16-mer. Selected NLMOs from (c) the monomer and (d) the 16-mer for site N1 and from (e) the monomer and (f) the 16-mer for site N2. These NLMOs are discussed in section 4.3. For clarity, the entire cluster is not displayed, and only molecules that contain the nitrogen of interest are shown using full color.

reduction of the absolute magnitude of V_{33} in the 16-mer compared to the monomer. The LP(N) MO is roughly the same shape in the monomer and 16-mer, but with slightly more localization of the MO at the N2 atom in the former (see Supporting Information for the decomposition of the nitrogen lone pairs in terms of atomic orbitals). In addition, the $\sigma(\mathrm{N-C})_\mathrm{B}$ MOs are also very similar. Despite the comparable shapes of the MOs in the monomer and 16-mer, V_{22} is oriented perpendicular to the plane in the monomer (the two $\angle(V_{22}-\mathrm{N}-\mathrm{C})$ for the adjacent ring carbons are 84.8° and 95.6°), whereas V_{11} is in this position in the 16-mer (the analogous two $\angle(V_{11}-\mathrm{N}-\mathrm{C})$ are 88.4° and 91.1°). Both EFG tensors are relatively close to axial symmetry (meaning that V_{11} and V_{22} are similar to one another), so the difference in orientation between these two components resulting from intermolecular contacts is not too surprising. The components directed out of the plane (V_{22} monomer, V_{11} 16-mer) also have large negative contributions from $\pi(\mathrm{N-C})$ MOs and numerous other MOs below the threshold (for listing); however, these are offset by large positive contributions from $\sigma(\mathrm{N-C})$ and LP(N) MOs and are therefore positive in sign. The components normal to the lone pair (V_{11} monomer, V_{22} 16-mer) do not have negative $\pi(\mathrm{N-C})$ MO contributions; rather they are dominated by negative σ and positive π and LP(N) contributions. It should also be pointed out that for the 16-mer there are small but significant negative and positive overall contributions to V_{11} and V_{22}, respectively, that undoubtedly arise from intermolecular interactions.

It is clear from these examples that an understanding of contributions from individual MOs to the EFG tensor is paramount in studying local and intermolecular interactions. 1,4-Dicyanobenezene provides an instance of a ^{14}N EFG tensor in a relatively "isolated" molecule in the solid state, while urea and imidazole demonstrate the sensitivity of the ^{14}N EFG tensor to intermolecular interactions such as hydrogen bonding and π-stacking, as well as near-, mid-, and longer range electrostatic components. A larger survey of numerous structural motifs is

Table 6. Calculated Nitrogen EFG Tensor Components for Imidazole Site N2 in Monomer and 16-Mer Structures

	V_{33} (au)	V_{22} (au)	V_{11} (au)	C_Q (MHz)	η_Q
Monomer	-0.857	0.442	0.415	-4.11	0.03
16-mer	-0.653	0.399	0.254	-3.14	0.22
	$V_{33}{}^{M}$-$V_{33}{}^{C}$	$V_{11}{}^{M}$-$V_{22}{}^{C}$	$V_{22}{}^{M}$-$V_{11}{}^{C}$		
Δ(Monomer-Cluster)[1]	-0.203	0.016	0.188	-0.97	-0.19

NLMO Contributions to V_{33} (in au)[2]

	Monomer		16-mer		Δ(Monomer-Cluster)
	Lewis	non-Lewis	Lewis	non-Lewis	
$\sigma(N\text{-}C)_A$	0.123	0.007	0.102	0.019	0.009
$\sigma(N\text{-}C)_B$	0.196	0.010	0.249	0.020	-0.063
$\pi(N\text{-}C)_A$	-0.014	0.147	-0.028	0.155	0.006
$\pi(N\text{-}C)_B$	1.149	-0.029	1.213	-0.028	-0.065
LP(N)	-2.483	0.068	-2.605	0.175	0.015
Sum	**-1.029**	**0.203**	**-1.069**	**0.341**	**-0.098**
Σ(small terms)[3]	-0.031		0.075		-0.105

NLMO Contributions to V_{22}(monomer) vs. V_{11}(cluster) (in au)

	Monomer (V_{22})		16-mer (V_{11})		Δ(Monomer-Cluster)
	Lewis	non-Lewis	Lewis	non-Lewis	
σ(N-H)	0.965	-0.019	1.029	-0.007	-0.076
σ(N-C)	0.981	-0.023	1.034	-0.010	-0.066
$\pi(N\text{-}C)_A$	-2.234	0.057	-2.398	0.057	0.164
$\pi(N\text{-}C)_B$	-0.022	-0.283	0.013	-0.303	-0.015
$\pi(N\text{-}C)_C$	0.020	-0.123	0.062	-0.105	-0.060
Core(C)			0.109	0.001	-0.110
Core(C)			0.122	0.001	-0.123
LP(N)	1.190	-0.029	1.291	-0.084	-0.046
Sum	**0.900**	**-0.420**	**1.262**	**-0.450**	-0.332
Σ(small terms)[3]	-0.038		-0.558		0.520

NLMO Contributions to V_{11}(monomer) vs. V_{22}(cluster) (in au)

	Monomer (V_{11})		16-mer (V_{22})		Δ(Monomer-Cluster)
	Lewis	non-Lewis	Lewis	non-Lewis	
σ(N-H)	-1.088	0.012	-1.130	-0.012	0.066
σ(N-C)	-1.177	0.012	-1.283	-0.010	0.128
$\pi(N\text{-}C)_A$	0.036	0.136	1.185	-0.029	-0.984
$\pi(N\text{-}C)_B$	1.085	-0.028	0.015	0.147	0.895
Core(C)			-0.107	-0.001	0.108
Core(C)			-0.101	0.000	0.101
LP(N)	1.293	-0.039	1.313	-0.091	0.032
Sum	**0.149**	**0.093**	**-0.108**	**0.004**	0.346
Σ(small terms)[3]	0.173		0.503		-0.330

[1] Differences between V_{ii} components with common alignments are presented here. Values in table cells with the same shading are compared above. See text for details. [2] Shaded regions of the NLMO lists contain values which are referred to directly in the text. [3] All terms greater than 0.100 au are included in the table. More distant molecular orbitals make small contributions to the EFG at the relevant nitrogen, and the sum of all these small terms (both Lewis and non-Lewis) is included here for completeness.

currently underway and should provide a means of determining the nature of intermolecular interactions in a broad array of nitrogen-containing systems.

5. Summary

We have acquired ultra-wideline static ^{14}N NMR powder patterns at 21.1 T in a piecewise fashion using the WURST-QCPMG experiment, with only half of each pattern needing to be acquired. While ^{15}N NMR of isotopically enriched samples remains the easiest way of measuring nitrogen chemical shifts and CSA, our approach allows the accurate measurement of EFG tensor parameters and is not inherently limited in the range of C_Q values that may be studied. We have shown that sites with very similar EFG parameters may be distinguished in certain cases, depending primarily on the S/N ratio of the spectrum, which in turn depends on the relaxation characteristics of the sample. Long T_2 and short T_1 values are ideal, allowing many echoes to be obtained with a short recycle delay, as was the case for the dicyanobenzene samples.

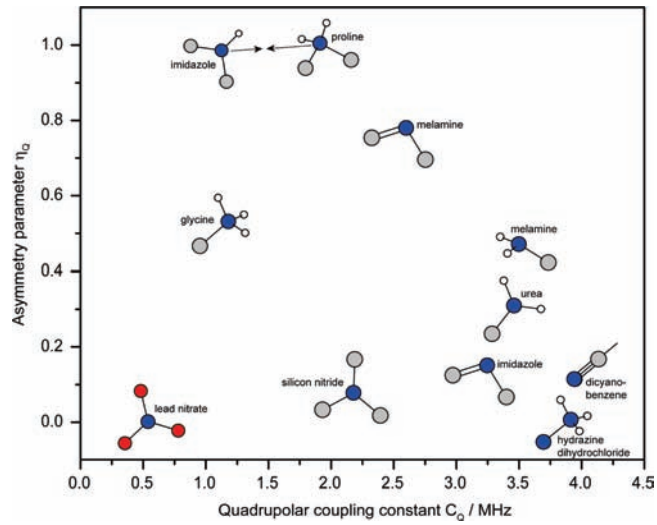

Figure 15. A visual summary of the EFG parameters determined for various nitrogen environments studied here and in previous work.[27]

Figure 15 serves as a visual summary of EFG parameters determined for the various nitrogen environments studied here and in our previous work.[27] The various common structural motifs of nitrogen clearly show a wide range of both quadrupolar coupling constants and asymmetry parameters, which bodes well for the utility of the experimental approach described here to distinguish different nitrogen environments in samples featuring multiple sites. It is evident, however, that not only can very different nitrogen environments give rise to similar EFG parameters (e.g., the imidazole N1 site and the nitrogen site in proline), but also that seemingly similar nitrogen environments can produce EFG parameters that differ significantly. Thus, a consideration of both the local molecular structure and, crucially, intermolecular effects such as hydrogen bonding and the extended crystal lattice, is essential in rationalizing the origin of these parameters. DFT calculations such as those presented here are therefore vital in interpreting the experimental results.

Plane-wave DFT calculations of ^{14}N EFG parameters and chemical shifts in infinite periodic systems show remarkable accuracy over a wide range of values, allowing comparison with experimental measurements, assignment of parameters to the correct crystallographic sites, and the determination of the orientation of interaction tensors in the molecular frame. Optimization of proton positions resulted in more accurate results overall, but is not required in every case (e.g., where accurate positions were already determined using neutron techniques, as was the case for imidazole). Larger discrepancies between the calculated and experimental ^{14}N C_Q values were observed in urea and hydrazine dihydrochloride, in which various dynamic modes are known to occur. Given the very good agreement for this parameter in the other systems studied, such discrepancies might therefore be useful as a general indicator of the presence of dynamics.

Dynamics and relaxation effects can play a very important role in determining the nature of the WURST-QCPMG spectrum. We very recently demonstrated that molecular dynamics which modulate the magnitude or orientation of the ^{14}N EFG tensor can be probed qualitatively and quantitatively via their effect on the powder line shapes as a direct analogy of more commonly used ^{2}H experiments.[28] Herein we have identified a second mechanism by which local dynamics can affect the ^{14}N spectrum; orientation-dependent modulations of N−H dipolar

couplings can cause an observable anisotropy in QCPMG enhancement even when the EFG tensor remains unaltered. We also observed a significant difference in T_2 for the two types of nitrogen environments in melamine. This latter effect resulted in only the ring sites being observed in the WURST-QCPMG spectrum, while line shapes from both the ring and amine sites could be simulated on the basis of the WURST-echo spectrum. These various relaxation phenomena provide a potentially useful means of probing dynamics, and even the possibility of spectral editing and site differentiation, but they also serve as a cautionary tale: NMR spectroscopists using the QCPMG protocol purely for signal enhancement purposes must take such effects into consideration when interpreting their spectral line shapes.

Finally, detailed analyses of EFG tensor orientations and contributing NLMOs utilizing DFT calculations on isolated molecules and larger clusters have provided a first glimpse of an intuitive means of probing intermolecular interactions on the basis of variations in ^{14}N EFG tensor parameters. Given the importance of nitrogen in many aspects of synthetic chemistry, structural biochemistry, supramolecular chemistry, and materials science, there is great potential for the combination of these experimental and theoretical methods to assist in better defining such interactions and to aid in the rational design of new materials.

Acknowledgment. The National Ultra-High Field NMR Facility for Solids, Ottawa (www.nmr900.ca), is acknowledged for providing access to the 900 MHz facility and also for the use of the CASTEP software. In particular, Victor Terskikh and Eric Ye are acknowledged for assistance with the NMR experiments, and Paul Morris is thanked for help with probe construction and modifications. We also thank Prof. Robert Vold for providing a copy of EXPRESS, and Prof. David Bryce for providing a copy of EFGShield. R.W.S. thanks the Natural Sciences and Engineering Research Council (NSERC), the Canadian Foundation for Innovation (CFI), the Ontario Innovation Trust (OIT), and the University of Windsor for financial support, as well as the Ontario Ministry of Research and Innovation for an Early Researcher Award. J.A. thanks the National Science Foundation (CHE 952253 and 447321) and the U.S. Department of Energy (DE-SC0001136) for financial support, and the Center for Computational Research at Buffalo for supporting part of the computations carried out for this work.

Supporting Information Available: Discussion of symmetry of ^{14}N NMR powder patterns; *k*-points and cutoff energies for the CASTEP calculations; comparison of fits of ^{14}N transverse relaxation in melamine; discussion of DFT cluster calculations; further molecular/atomic orbital analysis of EFG tensors in 1,4-dicyanobenzene, urea, and imidazole. This material is available free of charge via the Internet at http://pubs.acs.org.

JA108181Y